Full Length Article

Strain partitioning and strain localization in medium manganese steels measured by in situ microscopic digital image correlation

Aniruddha Dutta[a], Dirk Ponge[a,*], Stefanie Sandlöbes[a,b], Dierk Raabe[a]

[a] Department of Microstructure Physics and Alloy Design, Max-Planck-Institut für Eisenforschung GmbH, Max-Planck-Str. 1, 40237 Düsseldorf, Germany
[b] Institut für Metallkunde und Metallphysik, RWTH Aachen, 52056 Aachen, Germany

ABSTRACT

In situ microscopic-digital image correlation (µ-DIC) is used to investigate the strain partitioning and strain localization behavior in a medium manganese steel. Continuous yielding results from strain partitioning with higher strain in the reverted austenite (γ_R) islands and less strain in the tempered martensite (α'_{temp}) matrix, both in hot and cold rolled material. µ-DIC experiments are performed to further understand the effects of texture and grain morphology on strain partitioning which cannot be locally resolved through high resolution x-ray or neutron diffraction experiments. Apart from strain partitioning, strain localization is observed in hot rolled samples within colonies of lamellar γ_R islands. This localization does not only depend on the crystallographic orientation, but also on the spatial alignment of an austenite island relative to the loading direction. The effects of texture, spatial and colony alignment are interpreted within the concept of a relative grain size effect resulting in different yield stresses in the hot and cold rolled samples showing continuous yielding. Strain partitioning and strain localization based on texture and spatial alignment can be extended to numerous dual phase morphologies with similar texture, colony and spatial alignment effects.

1. Introduction

Due to increasing property requirements for metallic materials in automotive applications, there is an increasing interest in medium Mn steels which fall under the 3rd generation of advanced high strength steels. With a manganese content between 3 and 12 wt.%, medium Mn steels show promising property combinations of high to ultra-high strength at sufficient total elongations [1–6]. The ultra-fine grain (UFG) microstructure of these steels is obtained through an intercritical annealing treatment, resulting in a complex multi-phase microstructure consisting of austenite, martensite/ferrite and sometimes delta ferrite. Especially the austenite islands contribute to the material's ductility due to the higher strain hardenability enabled by enhanced dislocation accumulation, TRIP and/or TWIP effects. Careful compositional alloy design and appropriate selection of the intercritical annealing temperature and thermomechanical treatment results in the formation of different types of beneficial microstructures at room temperature [2,7,8]. Austenite growth during the intercritical annealing process takes place with the composition given by local equilibrium partitioning [9]. Accordingly, selecting different intercritical annealing temperatures results in austenite having different compositions and, hence, stacking fault energy values, thus affecting its deformation mechanisms and strain hardening response. The complex strain partitioning phenomena occurring among the various phases upon mechanical loading is the key to better understand the underlying mechanisms and tailor the mechanical behavior of medium Mn steels, thus, allowing further tuning of this emerging material class.

Several studies reveal strain partitioning effects among the phases in advanced high strength steels where typically a heterogeneous strain distribution was observed [10–12]. In medium Mn steels it was suggested that the strain was localized in the coarser ferrite grains although exact correlation to the phase map was not shown [10]. The strain partitioning between austenite and martensite has been reported to be responsible for the enhanced plasticity of medium Mn steels. Observation of deformation partitioning in a TRIP-maraging steel conducted by in situ high resolution EBSD, have shown that the local strain preferentially partitions to small reverted austenite grains (0.1–0.3 µm²) causing their strain-induced phase transformation to martensite at global nominal strains of 2.3% [13]. However, larger reverted austenite grains (0.4–4 µm²) interestingly remained untransformed, indicating that the strain seems to be preferentially accommodated by the small austenite grains [13]. These experiments were carried out to determine the strain localization behavior within differently sized austenite grains, however, the actual local strain values were not quantified. An early attempt to study also the local strain partitioning between different phases has been conducted using in situ neutron diffraction on cold rolled medium Mn steel

* Corresponding author.
E-mail addresses: ponge@mpie.de, d.ponge@mpie.de (D. Ponge).

[14]. Measurements of the phase fractions, phase specific lattice strains and the corresponding peak broadening have been used to understand the yielding phenomena and plastic deformation of the phases. The authors reported that yielding after annealing at 650 °C was controlled by the austenite which deforms through the TRIP-mechanism resulting in a high work hardening rate [14]. Annealing at 600 °C has been reported to cause pre-dominant deformation of recrystallized ferrite resulting in an initial yield point elongation [14].

A constitutive model on a cold rolled medium Mn steel with both twinning induced (TWIP) and transformation induced (TRIP) plasticity mechanisms in a finite element framework has shown alternating characteristics in strain partitioning among the phases [15,16]. With the TWIP plus TRIP effect turned on in the model, the austenite strain hardened at a low global strain as it twinned or transformed to martensite, thus considering the austenite to be the softer phase at the beginning of plastic flow [15]. At higher strains, a shift of strain partitioning from the austenite to the ferrite was observed [15]. According to finite element analysis (FEM), the austenite and the freshly formed strain-induced martensite showed a certain saturation of strain inside of the austenite and accommodation of strain upon progressive loading within the initially present martensite at an intermediate nominal strain of 10% [15].

The present investigation aims to measure the partitioning of strain between the various constituent phases in a medium Mn steel using a micro digital image correlation (μ-DIC) approach [17–19]. The approach is similar to the one described in [18]. Our study reveals that continuous yielding in hot and cold rolled medium Mn steel follows from the fact that the von Mises strain carried by the reverted austenite exceeds that which is accommodated by the tempered martensite matrix. Strain localization is clearly observed in the hot rolled medium Mn steel due to the elongated topological alignment of the reverted austenite grains.

2. Experimental procedure

2.1. Material selection

The current study was conducted on a medium Mn steel with a composition of Fe-0.05%C-12%Mn-3%Al (all compositions in wt.%, here and below) exposed to intercritical annealing at a temperature of 555 °C. The composition and intercritical annealing temperature were selected to adjust a stacking fault energy (SFE) of 25 mJ/m^2 in the austenite at room temperature [20]. The corresponding equilibrium austenite volume fraction amounts to 40% [21]. The Koistinen and Marburger equation [22] was used to predict the composition-dependent M_s temperature to predict the thermal stability of the austenite and its ability to transform back to fresh martensite during cooling.

2.1.1. Material processing

The material was molten in a vacuum induction furnace and cast into a Cu mold. The central fiber of the as-cast block containing macro-segregation was removed and the two remaining blocks were cut into two sets of samples. One set of samples was hot rolled at 1150 °C down to a thickness of 8.2 mm corresponding to an engineering thickness reduction of 80%. The rolled sample was further homogenization annealed at 1100 °C in argon atmosphere for 2 h and subsequently water quenched. The other sample set was hot rolled at 1150 °C to a final sheet thickness of 2.5 mm in 16 rolling passes. Each rolling pass resulted in a thickness reduction of 10%. The hot-rolled sample was then homogenization annealed at 1100 °C in argon atmosphere for 2 h and water quenched. Subsequently, the sample was cold rolled to a thickness reduction of 50% resulting in a final sheet thickness of 1.25 mm. Fig. 1 shows the processing parameters for both the hot and cold rolled samples. All samples were then cut into tensile test specimens (see Section 2.3) and heat treated separately (see Section 2.2).

2.2. Heat treatment

The hot rolled samples were annealed at 930 °C for 10 min above the A_{c3} temperature (830 °C) and subsequently quenched to 20 °C. The martensite finish (M_f) temperature of the material was 35 °C. The samples were then intercritically annealed at 555 °C for 12 h as shown in Fig. 1. The austenite formed during this treatment is referred to as reverted austenite (γ_R). The heating rate was set to 10 K/s and the cooling rate to −100 K/s for all heat treatments. The martensite present after the intercritical heat treatment is referred to as tempered martensite (α'_{temp}) to differentiate it from the newly formed deformation-induced martensite (α'_{fresh}) that formed from the transformed γ_R during deformation. The hot rolled and intercritically annealed samples from here on are referred to as HRA.

The cold rolled samples were intercritically annealed at 555 °C at 10 K/s, annealed at 555 °C for 12 h and quenched to room temperature
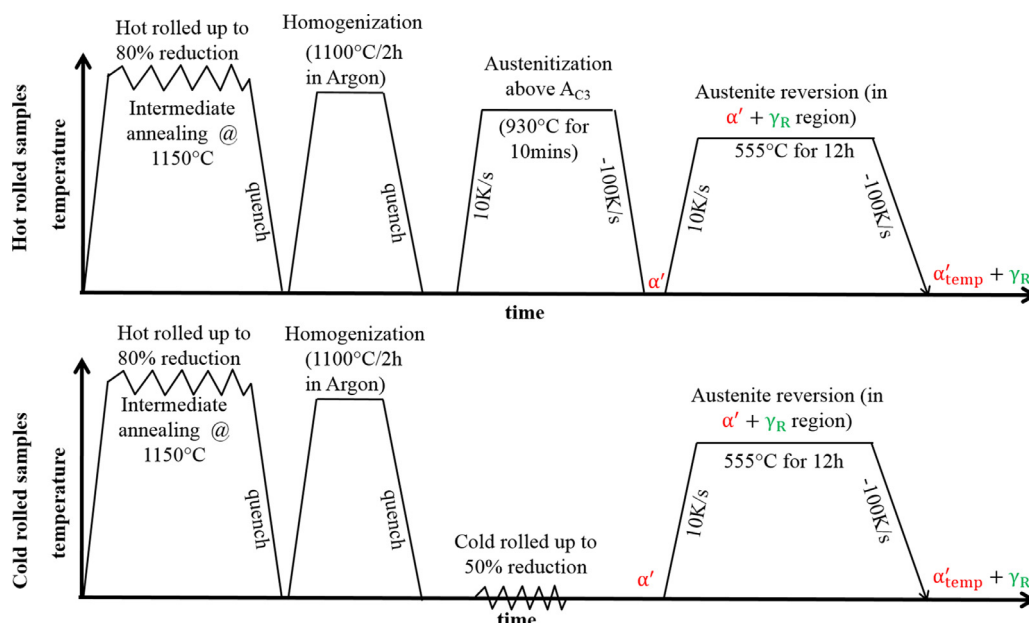

Fig. 1. Processing parameters of the hot rolled and cold rolled materials investigated.

at −100 K/s for the intercritical annealing process. The cold rolled and intercritically annealed samples from here on are referred to as CRA.

2.3. Mechanical testing and microstructure characterization

Room temperature uniaxial tensile tests of dog-bone shaped samples with a gauge length of 4 mm, machined along the rolling direction, were conducted at an initial strain rate of 10^{-3} s^{-1} using a Kammrath and Weiss tensile stage. Electron backscatter diffraction (EBSD) measurements were carried out using an EDAX/TSL system at a step size of 50 nm in a Jeol JSM-6500F FEG-SEM scanning electron microscope (SEM) operated at 15 kV. The volume fractions of the different phases in the annealed specimens were determined in situ by X-ray diffraction (XRD; Bruker D8) using a Co-Kα radiation source ($\lambda = 1.7889$ Å). Phase fractions were calculated using the integrated intensities of all diffracted peaks. A miniature tensile test device mounted on the system using a flat tensile test sample was used to measure the phase fractions after every 2% strain step. Electron channeling contrast imaging (ECCI) analysis was performed using a Zeiss Merlin SEM, equipped with a field emission gun and a solid state four-quadrant detector. ECCI was conducted at 30 kV acceleration voltage at a working distance of approximately 6 mm.

In situ strain partitioning tensile tests were carried out in a Zeiss 1540XB Crossbeam SEM. The tensile specimens had gauge dimensions of $1 \times 0.5 \times 0.4$ mm^3. An EBSD scan was first performed followed by introducing focused ion beam (FIB) markers of the dimension of 1 μm, placed at least 10 μm away from the scanned region so that they could be identified after colloidal silica particle deposition. The drop casting technique was used to deposit a mono-layer of colloidal silica particles on the polished sample surface [18,23]. Nano-sized SiO$_2$ particles having an average size of 34 nm ± 29 nm were used with an average particle spacing of 25 nm. Colloidal silica was used as marker substance for this experimental set up to achieve a high spatial resolution at negligible interference with the electron beam. When using silica particles no heat treatment is required for particle deposition as compared to alternative methods using solid state dewetting [24], Pt [25] or Au deposition [26–28] where certain post heat treatments need to be applied for creating adequate marker patterns. The tensile test specimens were deformed stepwise using a Kammrath & Weiss tensile stage at 1 μm/s constant cross head speed which corresponds to an initial strain rate of 10^{-3} s^{-1}. The in-lens secondary electron (SE) detector in combination with a small aperture (30 μm) and low acceleration voltage (1.5 kV) was used to obtain a high spatial resolution and reducing topological effects arising from surface tilts. SE images of 3072×2304 pixels resolution were taken at every 2% increase in strain followed by processing of the images using the Aramis software (V6.3.0, GOM GmbH) [29,30]. The facet size were set to the same value as the EBSD step size (50–60 nm) enabling to achieve a stochastic pattern structure within a facet while the facet overlap was kept at a default of 20–25%.

3D EBSD was also carried out on a Zeiss 1540XB Crossbeam SEM. Gallium ion milling using a 30 KeV acceleration voltage was used to remove 15 successive through-thickness layers. A tilt set up was used as described in detail by Zaefferer et al. [31,32]. EBSD scans were collected before each slice and analyzed using an EDAX/TSL system at a step size of 50 nm. Each milling step was set to 50 nm thus providing a 50 nm step size in all 3 dimensions. 3D reconstruction was carried out using the software package QUBE, version 2.0.10, where the details are described by Konijnenberg et al. in [33].

3. Results

### 3.1. Mechanical response and crystallographic texture

Before intercritical annealing, no retained austenite was detected in the martensitic microstructure by EBSD using a step size of 50 nm. After intercritical annealing reverted austenite (γ_R) was observed. The hot

rolled and cold rolled samples after intercritical annealing are referred to as HRA and CRA, respectively. Fig. 2 shows the phase and inverse pole figure (IPF) maps of the HRA (a) and CRA (b) samples after intercritical annealing for 12 h. Both samples contain γ_R and tempered martensite (α'_{temp}). The γ_R in the HRA sample has the same crystallographic orientation within a prior austenite grain [34,35]. However, the γ_R in the CRA sample reveals a deformation-induced orientation spread. Further, differences in the morphology of γ_R are evident between the HRA and CRA samples. The γ_R in the HRA sample has a lamellar morphology, being larger in two dimensions and smaller in the third. The ratio of the larger to the smaller dimensions amounts to 5:1. This lamellar morphology is attributed to the nucleation and growth of γ_R from and along the lath martensite boundaries. Packets of martensite within a prior austenite grain contain γ_R lamellae with the same crystallographic orientation but different spatial alignments. Fig. 2(a) shows such regions in the γ_R IPF map. Regions 1, 2 and 3, highlighted by the white boxes, have the same γ_R crystallographic orientation, as seen in the IPF. The spatial alignments of the γ_R lamella are different in the three regions. Specifically, in region 2 the lamella structure is seen plane-on, in regions 1 and 3 the lamellar of γ_R are visible edge-on. Consequently, the γ_R in regions 1, 2 and 3 have the same grain morphology (lamellar) and the same crystallographic orientation but different spatial alignments. The γ_R in the CRA sample assumes a mixture of globular and ellipsoidal morphology, with the ellipsoidal morphology being larger in one dimension and smaller in the other two. To visualize the morphological differences, Fig. 2 (c and d) shows snapshots of the 3D EBSD data set (Supplementary Movie 1 and 2 in the supplementary material), depicting the γ_R in terms of IPF for the HRA and CRA samples. The lamellar morphology of γ_R is shown in Fig. 2(c) (Supplementary Movie 1 in the supplementary data) highlighting two different γ_R packets with different spatial alignment but the same crystallographic orientation, see also the schematic inserts. The deformation induced texture spread of γ_R in CRA material can be seen in Fig. 2(d) (Supplementary Movie 2 in the supplementary data) showing a different morphology than in the HRA state. Fig. 3(a) shows the engineering stress strain curves of the HRA and CRA samples. The data are presented along with their individual volume fraction of α'_{temp}, fresh martensite (α'_{fresh}) (data points) and γ_R (dashed lines), measured by in situ XRD with respect to the engineering strain. No epsilon martensite was detected using XRD. Both, the HRA and CRA samples show continuous yielding. The CRA material has a higher yield stress (YS) of 625 MPa than the HRA material which has a YS of 520 MPa. The ultimate tensile stresses (UTS) of the HRA and CRA materials are 690 MPa and 773 MPa, at 18.5% and 15.5% uniform elongation (UE), respectively. The volume fraction of γ_R in the HRA material decreased from 34% in the undeformed state to 24% near necking. For the CRA material, the volume fraction of γ_R decreased from 26% in the undeformed state to 19% close to necking. It is observed that the volume fraction of γ_R in the HRA sample started decreasing from a global engineering strain of 2% whereas in the CRA sample the volume fraction of γ_R started to decrease from 11% global engineering strain. Fig. 3(b) depicts the true stress-strain and corresponding strain hardening curves of the HRA and CRA material. The CRA material exhibits a more pronounced continuous yielding than the HRA material as can be seen from the strain hardening curves between 2% and 5% true strain.

3.2. Strain partitioning

Fig. 4 shows a phase map of the HRA material displaying the spatial distribution of γ_R and α'_{temp} (a) and local von Mises strain maps (b–e) corresponding to this region at certain global strains, highlighted in the engineering stress strain curve (f). The strain maps are plotted as von Mises strain as it has a direct correlation to the density of geometrically necessary dislocations. An inhomogeneous strain map is seen where areas of high von Mises strain within the strain maps is observed to correspond to γ_R regions as seen in the phase map, Fig. 4(a), although an
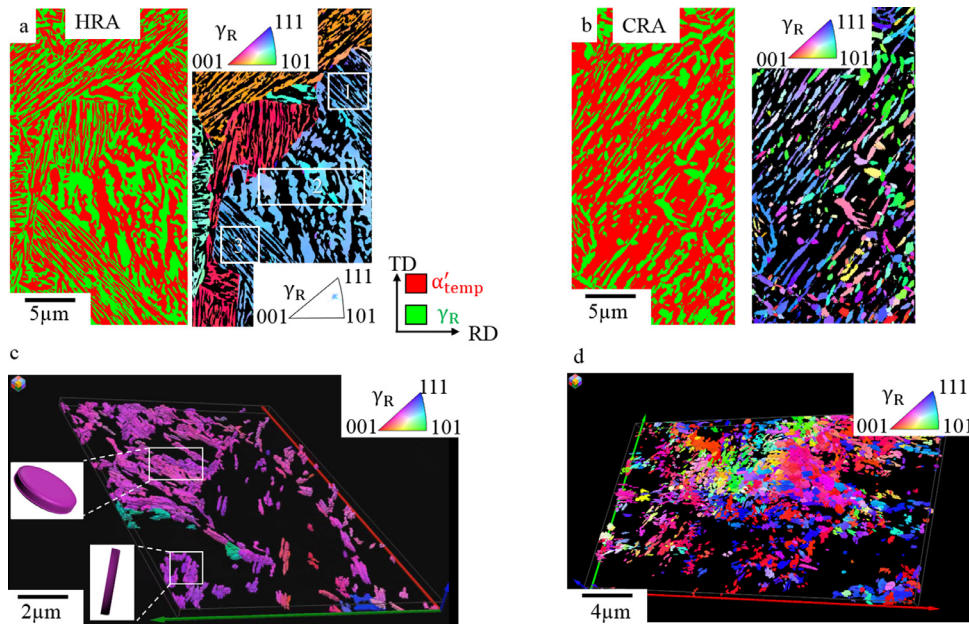
Fig. 2. Phase maps of γ_R and α'_{temp} and corresponding inverse pole figure (IPF) maps highlighting γ_R of the (a) HRA and (b) CRA material. 3D EBSD IPF snapshots of γ_R in (c) HRA and (d) CRA material (Supplementary Movie 1 and 2 in the supplementary data). γ_R: reverted austenite; α'_{temp}: tempered martensite; HRA: hot rolled and intercritically annealed; CRA: cold rolled and intercritically annealed.
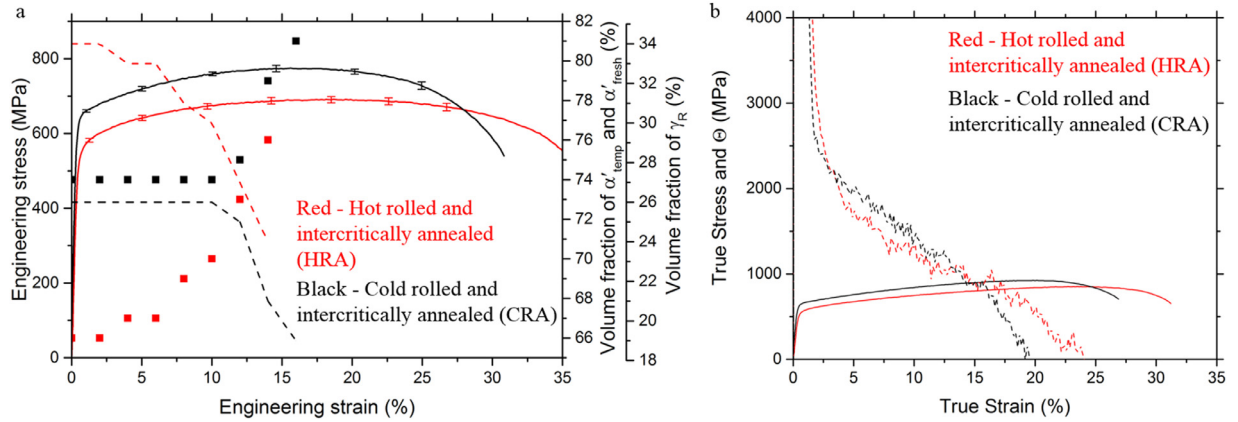

Fig. 3. (a) Engineering stress strain curves of the HRA and CRA samples (3 sets showing the scatter data) along with changes of the γ_R and α'_{temp} fraction vs. strain. (b) True stress strain curves and corresponding strain hardening curves of the HRA and CRA samples.). γ_R: reverted austenite; α'_{temp}: tempered martensite; HRA: hot rolled and intercritically annealed; CRA: cold rolled and intercritically annealed.

exact one to one correlation is not possible due to the small grain size. Fig. 4(g) displays the local von Mises strain along the black dashed arrow drawn in the phase map in Fig. 4(a) at various global strains. The graph clearly reveals that at global strains of up to 7.1%, the γ_R islands show high local von Mises strain levels of up to 15% while the local strain in the α'_{temp} regions is significantly lower. This is similar to the strain partitioning behavior observed using neutron diffraction in hot rolled medium manganese steels [36]. It should be noted that γ_R is metastable at room temperature and, hence, a driving force exists for deformation twinning or strain-induced martensitic transformation to α'_{fresh} depending on the magnitude of the SFE value [21]. Thus, initial γ_R regions in the undeformed microstructure are here denoted as γ_R / α'_{fresh} regions as it was not possible to determine the transformation to α'_{fresh} during in situ straining. The transformation of γ_R to α'_{fresh} would also result in a shape distortion which is included in the von Mises strain as it is comprised of dislocations and shape-change induced strains within the γ_R. At global strains above 10.2%, α'_{temp} shows some local von Mises strain which increases with increasing global strain. However, the local von

Mises strain within α'_{temp} does not reach values close to the local von Mises strain values of γ_R / α'_{fresh} at global strains up to 27.8%.

Fig. 5 shows of large area IPF maps of γ_R (a) and α'_{temp} (b) in a HRA sample indicating the prior austenite grain boundaries and corresponding von Mises strain maps at certain global strains (c–f). To obtain a high resolution strain image over a large area, the map was subdivided into 8 sections and images were captured for each section individually during the in situ test. Each individual section was processed and stitched together for each global strain measured, giving a high resolution image of a large area. At a global strain of 4.1%, some strain localization is observed at the prior austenite grain boundary, Fig. 5(d). As observed in Fig. 4, the local von Mises strain during the early stages of deformation, i.e. below a global strain of 7.1%, are assumed to be concentrated in the γ_R grains and are then taken up by α'_{temp} and γ_R / α'_{fresh}. The highly strained areas in Fig. 5 (c–e) are occurring within the γ_R and α'_{temp} grains with an inhomogeneous spread. Apart from strain partitioning to the γ_R at low global strains below 6.8%, preferred local straining of individual regions within a prior austenite grain is observed.
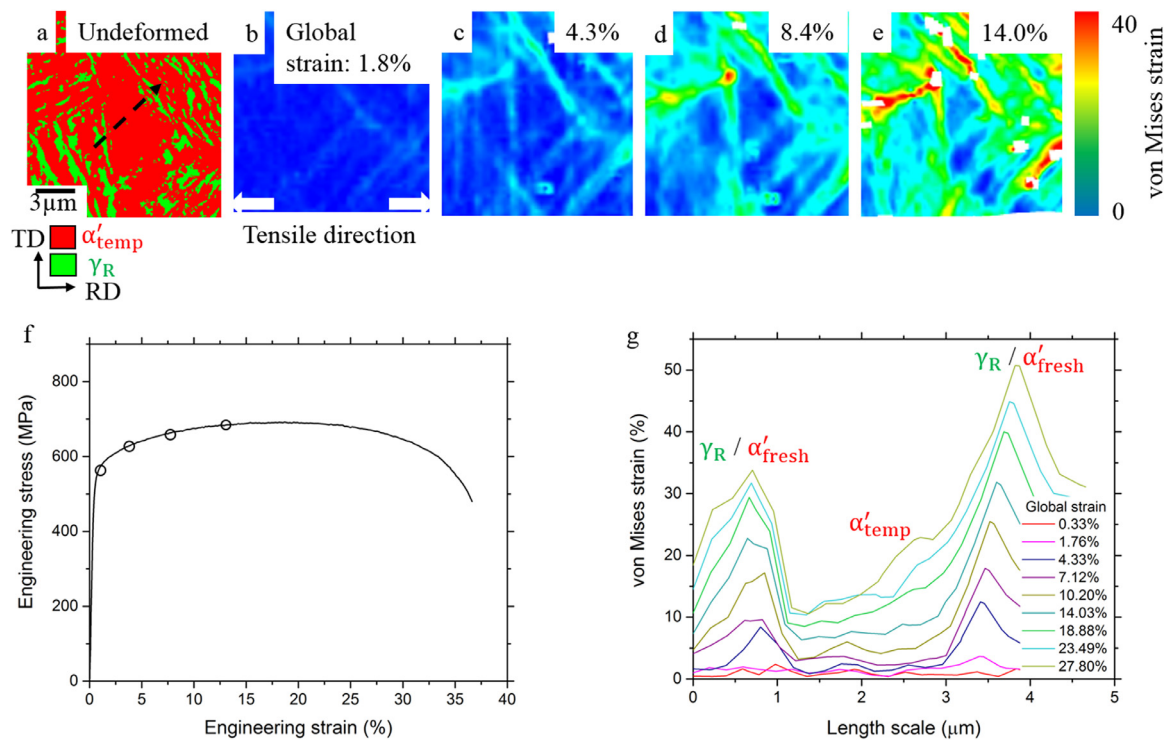
Fig. 4. (a) Phase map of γ_R and α'_{temp} in the HRA material and the corresponding von Mises strain maps at (b) 1.8%, (c) 4.3%, (d) 8.4% and (e) 14% global. (f) Corresponding strain values in the stress strain curve. (g) Local von Mises strains strain taken along the black dashed arrow in (a) with increasing global strain highlighting the γ_R/α'_{fresh} and α'_{temp} regions. γ_R: reverted austenite; α'_{temp}: tempered martensite; α'_{fresh}: fresh martensite, i.e. newly transformed martensite; HRA: hot rolled and intercritically annealed.
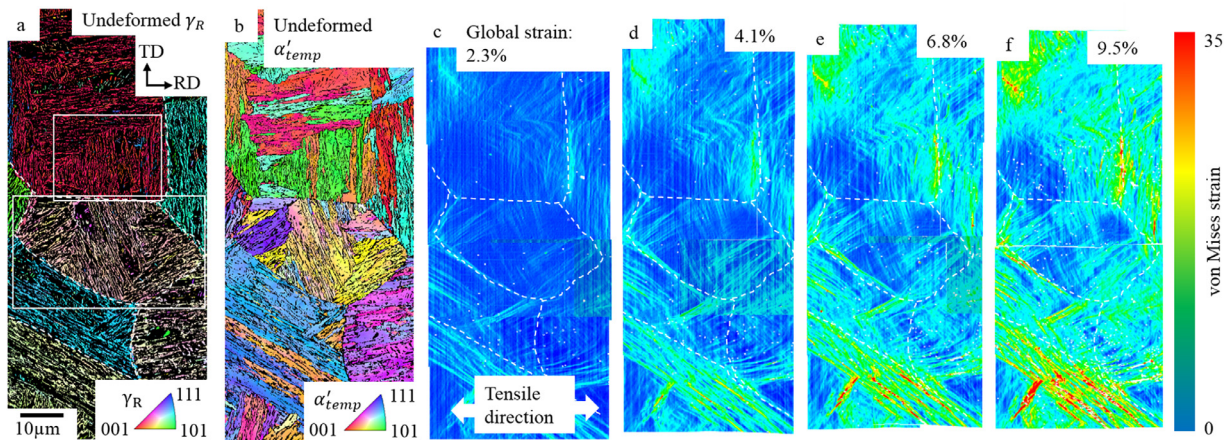
Fig. 5. Large area IPF maps of (a) γ_R and (b) α'_{temp} of the HRA material and the corresponding local von Mises strain maps at (c) 2.3%, (d) 4.1%, (e) 6.8% and (f) 9.5% global strain. γ_R: reverted austenite; α'_{temp}: tempered martensite; HRA: hot rolled and intercritically annealed.

Observations of specific regions in HRA samples are considered below based on spatial alignment and texture of both, the γ_R and α'_{temp}.

Case 1 – Importance of γ_R spatial alignment

Fig. 6 shows the region marked by the lower rectangle in the γ_R IPF map in Fig. 5(a) at higher magnification. γ_R and α'_{temp} IPF maps of the undeformed material are presented in Fig. 6(a) and (b), respectively. Fig. 6(c) shows the lamella loading angle of γ_R to the tensile axis[1] being parallel to the rolling direction (RD). To understand the influence

of the spatial alignment of the γ_R grains on strain localization, three areas have been considered individually, hereafter referred to as areas $1_{HRA\ Fig.6}$, $2_{HRA\ Fig.6}$ and $3_{HRA\ Fig.6}$ (Fig. 6(a) and (c)), all having the same crystallographic orientation of γ_R shown by the IPF in Fig. 6(a). The respective γ_R grains are in Kurdjumov-Sachs (K-S) orientation relationship (OR) to α'_{temp}. Based on this orientation relationship, the phase boundary plane was predicted for the three different areas giving the lamella plane normal angle to the sample normal direction (ND). This provides the angle of the γ_R lamella relative to the sample surface. The predicted phase boundary planes are shown as insets where the respective planes are highlighted in the corresponding crystallographic unit cells in Fig. 6(a) and (b) for the three areas. As seen from the insets, colonies of γ_R islands within areas $1_{HRA\ Fig.\ 6}$ and $3_{HRA\ Fig.\ 6}$ are inclined by 45° to RD (Fig. 6(c)) and the lamella normal is 48° to ND (blue

[1] The term "lamella loading angle" refers to the spatial arrangement of austenite lamellae and islands with respect to the global tensile loading axis when assuming an uniaxial stress state.
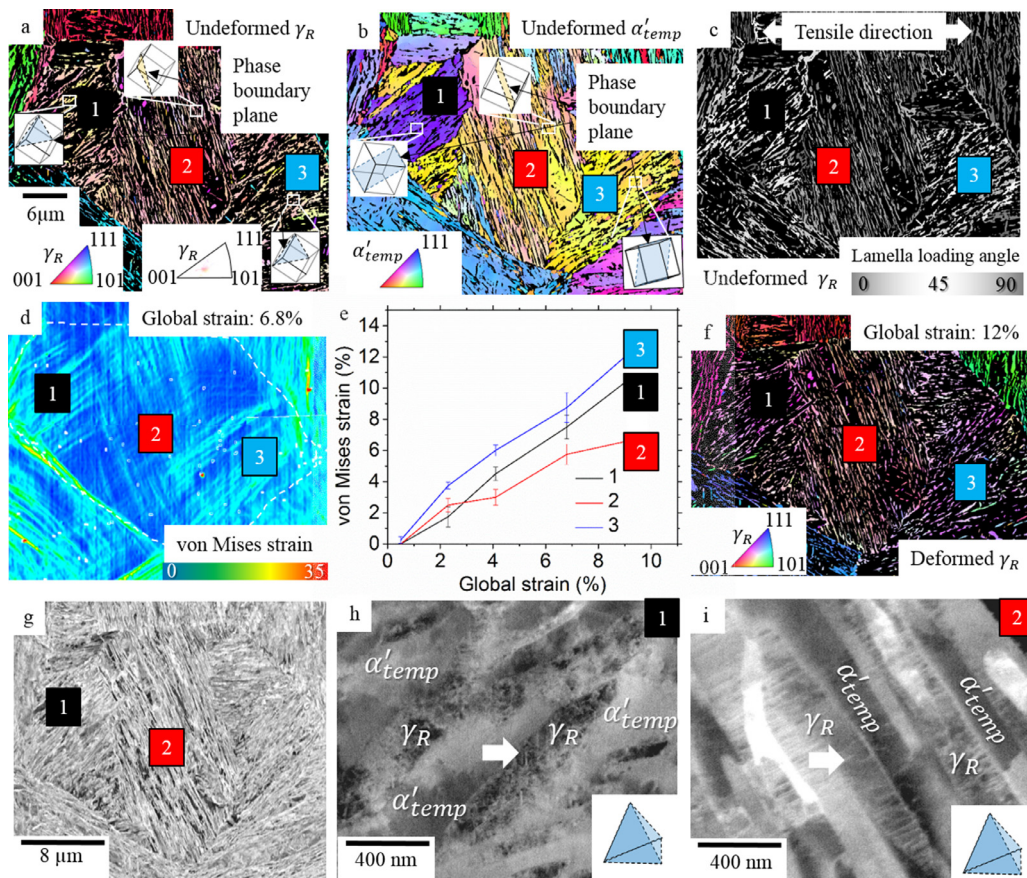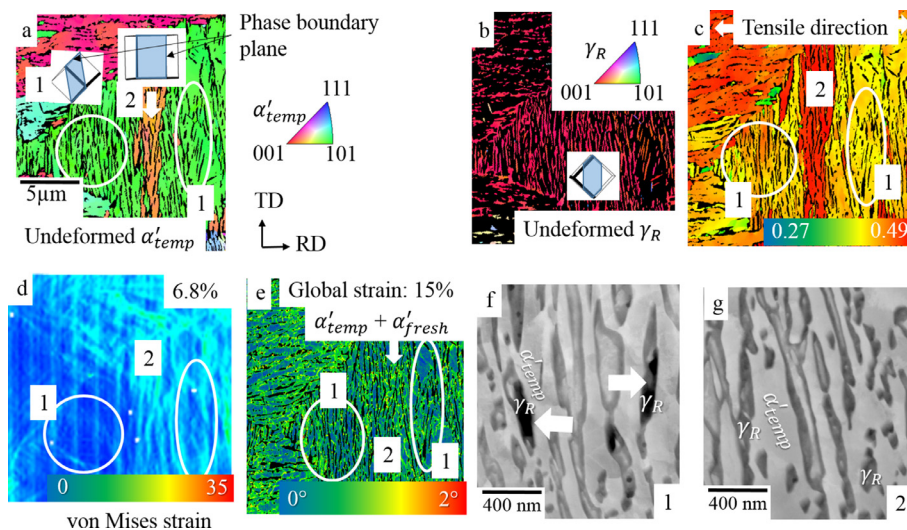
Fig. 6. Magnified images of the area marked by the lower rectangle in Fig. 5 highlighting (a) γ_R in un-deformed material in terms of an IPF map, (b) α'_{temp} IPF map of undeformed material, (c) corresponding loading angles to the tensile direction. Insets in (a) and (c) give the common phase planes between γ_R and α'_{temp} following the K-S relationship highlighting areas $1_{HRA\,Fig.\,6}$, $2_{HRA\,Fig.\,6}$ and $3_{HRA\,Fig.\,6}$. (d) Local von Mises strain map at 6.8% global strain. (e) Evolution of the local strain within the individual areas and corresponding γ_R area fractions up to 12% global strain (f) IPF map of γ_R in material deformed to 12% global strain. (g) ECCI images of the same area shown in (f) with high magnification images of (h) areas $1_{HRA\,Fig.\,6}$ (h) and $2_{HRA\,Fig.\,6}$ (i). γ_R: reverted austenite; α'_{temp}: tempered martensite. (For interpretation of the references to color in this figure, the reader is referred to the web version of this article.)

planes in the corresponding crystallographic unit cell) . At the same time, colonies of γ_R islands within area $2_{HRA\,Fig.\,6}$ are inclined by 60° to RD (Fig. 6(c)) and 78° to ND (yellow planes in the corresponding crystallographic unit cell). Fig. 6(d) shows the local von Mises strain map of the same microstructural region at a global strain of 6.8%. It is evident that higher local von Mises strains of up to 8% are present in areas $1_{HRA\,Fig.\,6}$ and $3_{HRA\,Fig.\,6}$, while area $2_{HRA\,Fig.\,6}$ exhibits lower von Mises strains of up to 5.5%. Although a grain resolved strain map could not be obtained because of the fine grain size, it is assumed from Fig. 4 and neutron diffraction experiments [36] that at early deformation states below 6% global strain, the von Mises strain is higher within the γ_R islands than in the α'_{temp} and deformation is take up by both the phases at higher global strains. Fig. 6(e) compares the von Mises strain of areas $1_{HRA\,Fig.\,6}$, $2_{HRA\,Fig.\,6}$ and $3_{HRA\,Fig.\,6}$ at different global strains within the γ_R and α'_{temp} colonies. Although areas $1_{HRA\,Fig.\,6}$ and $3_{HRA\,Fig.\,6}$ are surrounded by α'_{temp} with different crystallographic orientations, the local von Mises strains in the γ_R and α'_{temp} colonies of areas $1_{HRA\,Fig.\,6}$ and $3_{HRA\,Fig.\,6}$ show similar local von Mises strains. The Schmid factors for {110} <111> slip in α'_{temp} are similarly high with values close to 0.5 in all three areas. Fig. 6(f) shows the post-deformation IPF map of the γ_R grains at a global strain of 12%. Post-deformation EBSD analysis reveals a reduction of the γ_R area fraction of 25% in area $2_{HRA\,Fig.\,6}$ while a reduction in the γ_R area fraction of 38% and 36% is observed for areas $1_{HRA\,Fig.\,6}$ and $3_{HRA\,Fig.\,6}$, respectively. Thus, areas $1_{HRA\,Fig.\,6}$ and $3_{HRA\,Fig.\,6}$ which show higher local von Mises strains also show a higher fraction of strain induced $\gamma_R \rightarrow \alpha'_{fresh}$ transformation than area

$2_{HRA\,Fig.\,6}$. Similar observations were made in different areas as seen in Supplementary Figure 1 where two areas of γ_R (a and c) are compared with pre and post deformation IPF maps along with local von Mises strain maps (d). Fig. 6(g) provides ECCI images of the same area as Fig. 6(f) at a global strain of 12%. Fig. 6(h) and (i) are magnified images of Fig. 6(g) comparing areas $1_{HRA\,Fig.\,6}$ and $2_{HRA\,Fig.\,6}$ in higher detail. Fig. 6(h) displays a magnified image of area $1_{HRA\,Fig.\,6}$ showing different slip systems as highlighted by the solid white arrows with a high density of stacking faults, while in area $2_{HRA\,Fig.\,6}$ (Fig. 6(i)) only a single slip system is observed. Strain localization in the present case is consequently dependent on the spatial alignment of the γ_R and α'_{temp} within a packet as the γ_R crystallographic orientations are the same within a prior austenite grain. The γ_R colonies in the three areas are surrounded by different crystallographic orientations of α'_{temp} having similar Schmid factors for {110} <111> slip.

Case 2 – Role of the α'_{temp} crystallography at higher deformation states when the γ_R is not favorable (spatially) aligned for shear

Fig. 7(a) and (b) show IPF maps of undeformed α'_{temp} and γ_R in a HRA sample, where the corresponding region of interest is marked by the upper rectangle in the γ_R IPF map in Fig. 5(a). Two regions were selected, areas $1_{HRA\,Fig.\,7}$ (highlighted by the circle) and $2_{HRA\,Fig.\,7}$ (highlighted by the arrow), which have different crystallographic orientation of α'_{temp} but the same crystallographic orientation of γ_R, Fig. 7(b). Fig. 7(c) shows the Schmid factor map of the {110} <111> slip system of undeformed α'_{temp} with respect to the tensile direction. The α'_{temp} in area $2_{HRA\,Fig.\,7}$ shows a higher Schmid factor of 0.5 for {110} <111> slip than

Fig. 7. Magnified images of the area marked by the lower rectangle in Fig. 5 highlighting IPF map of undeformed α'_{temp} (a) and γ_R (b). Insets in (a) and (b) give the common phase planes between γ_R and α'_{temp} following the K-S relationship highlighting areas $1_{HRA\ Fig.\ 7}$ and $2_{HRA\ Fig.\ 7}$. Schmid factor map of α'_{temp} for {110} <111> slip (c). Von Mises strain maps of the same area at 6.8% global strains (d). KAM map of $\alpha'_{temp} + \alpha'_{fresh}$ (e) at 15% global strain. ECCI Images of area $1_{HRA\ Fig.\ 7}$ (f) and area $2_{HRA\ Fig.\ 7}$ (g). γ_R: reverted austenite; α'_{temp}: tempered martensite; α'_{fresh}: fresh martensite, i.e. newly transformed martensite.

area $1_{HRA\ Fig.\ 7}$ which has a Schmid factor of 0.3. Fig. 7(d) shows a local von Mises strain map highlighting areas $1_{HRA\ Fig.\ 7}$ and $2_{HRA\ Fig.\ 7}$. Area $2_{HRA\ Fig.\ 7}$ has a higher local von Mises strain than area $1_{HRA\ Fig.\ 7}$ as also evident from Fig. 5. Strain localization is observed at a global strain level of 6.8%, whereas in Case 1 strain localization started at a global strain of 4%. Fig. 7(e) presents KAM maps of α'_{temp} and α'_{fresh} at 15% global strain indicating higher KAM values in area $2_{HRA\ Fig.\ 7}$ than in area $1_{HRA\ Fig.\ 7}$. Pre- and post- deformation EBSD showed no significant change in γ_R area fraction. Thus most of the higher α' KAM values within area $2_{HRA\ Fig.\ 7}$ are resulting from deformation of α'_{temp} and not of α'_{fresh}. Fig. 7(f) and (g) show ECCI maps of areas $1_{HRA\ Fig.\ 7}$ and $2_{HRA\ Fig.\ 7}$. ECCI images were obtained by orienting the colony of γ_R grains into Bragg condition using the (1 1 1) **g**-vector. Some of the γ_R grains in area $1_{HRA\ Fig.\ 7}$ show no in-grain contrast differences indicating no residual defects in these grains, while the γ_R grains in area $2_{HRA\ Fig.\ 7}$ reveal deformation induced defect structures. In summary, area $1_{HRA\ Fig.\ 7}$ shows low local von Mises strains and some of the γ_R grains showed no residual defects. Also, the surrounding α'_{temp} reveals low KAM values. Area $2_{HRA\ Fig.\ 7}$ shows higher local von Mises strain than area $1_{HRA\ Fig.\ 7}$. In area $2_{HRA\ Fig.\ 7}$, the γ_R grains exhibit deformation induced defect structures and the surrounding α'_{temp} exhibited higher KAM values than those present in region $1_{HRA\ Fig.\ 7}$. Although the γ_R grains have the same crystallographic orientation and spatial alignment in areas $1_{HRA\ Fig.\ 7}$ and $2_{HRA\ Fig.\ 7}$, the strain localization seems to be controlled by the crystallographic orientation of the surrounding α'_{temp} when γ_R was not ideally oriented for shear.

Fig. 8 shows a phase map (a) and the corresponding local von Mises strain maps (b–e) at different global strains of a CRA sample. The respective global strain values are highlighted in the engineering stress-strain curve (f). In the CRA samples, larger γ_R grains or clusters of small γ_R grains next to each other form aligned, band-like structures. These areas can be correlated to regions of high local von Mises strain as evident from the highlighted areas both in the phase map and the von Mises strain maps. Fig. 8(g) shows the local von Mises strain of γ_R / α'_{fresh} and α'_{temp} with increasing global strain. These data were achieved by taking multiple sections from the local von Mises strain maps and identifying the γ_R and α'_{temp} areas. Similarly as has been observed in the HRA sample, the γ_R/α'_{fresh} islands show higher local von Mises strains than α'_{temp}.

4. Discussion

The aim of this study is to compare the deformation, strain partitioning and localization behavior in hot rolled (HRA) and cold rolled (CRA) and subsequently intercritically annealed medium Mn steel. The HRA material consists of lamellar γ_R grains while the CRA material possesses

a combination of ellipsoidal and globular morphology of γ_R grains. The alloy was designed to contain γ_R with an SFE of 25 mJ/m^2 at room temperature and a volume fraction of ∼40%. The strain partitioning behavior is discussed based on the schematic shown in Fig. 10.

4.1. Influence of intercritical annealing temperature

An intercritical annealing temperature of 555 °C was chosen for this study. We observed that both, HRA and CRA material, show continuous yielding at room temperature, Fig. 3(a). It was reported that hot rolled medium Mn steels show a continuous yielding behavior but that the same material, when cold rolled, tends to form Lüders bands causing a discontinuous yielding behavior [37,38]. Most of the intercritical annealing temperatures reported for cold rolled medium Mn steels were above 600 °C and only short annealing times were applied [37,39–42]. Generally, intercritical annealing of cold rolled samples leads to the formation of γ_R, tempering of α' or - particularly at higher annealing temperatures - to the recrystallization of α' resulting in the formation of equiaxed ferrite. Kernel average misorientation (KAM) analysis of the α'_{temp} present in CRA medium Mn steel intercritically annealed for 1 min to 15 h at 555 °C did not show significant changes in the KAM values, indicating that no recrystallization resulting in equiaxed ferrite formation took place although recovery might have occurred (Supplementary Fig. 2). Therefore, it is assumed that the differences in the yielding behavior of the CRA samples in this study when compared to results reported in the literature for similar materials and experiments is caused by lower flow stresses of the γ_R grains compared to α'_{temp}. When choosing intercritical annealing temperatures at which recrystallization of α'_{temp} starts, equiaxed ferrite forms resulting in yield point elongation. This has been assumed to be due to the lower flow stress of the fine equiaxed ferrite which has a low strain hardenability with nearly no accumulation of dislocations and easy dynamic recovery. The ferrite recrystallization kinetics follow an Arrhenius-type behavior [43,44]. Thus lowering the intercritical annealing temperature would result in an increased time for α'_{temp} recrystallization. It has been shown that discontinuous yielding disappears at intercritical annealing times of more than one hour and an intercritical annealing temperature of 555 °C [45]. It is therefore assumed that due to the low fraction of γ_R formed upon intercritical annealing for less than one hour, the discontinuous yielding behavior is resulting from recovered α'_{temp}. The disappearance of discontinuous yielding at longer annealing times is accordingly attributed to the increased volume fraction of γ_R which results in increased strain hardening and continuous yielding.

On the other hand, the fact that no Lüders bands were observed in cold rolled medium Mn steel which was exposed to high intercritical an-
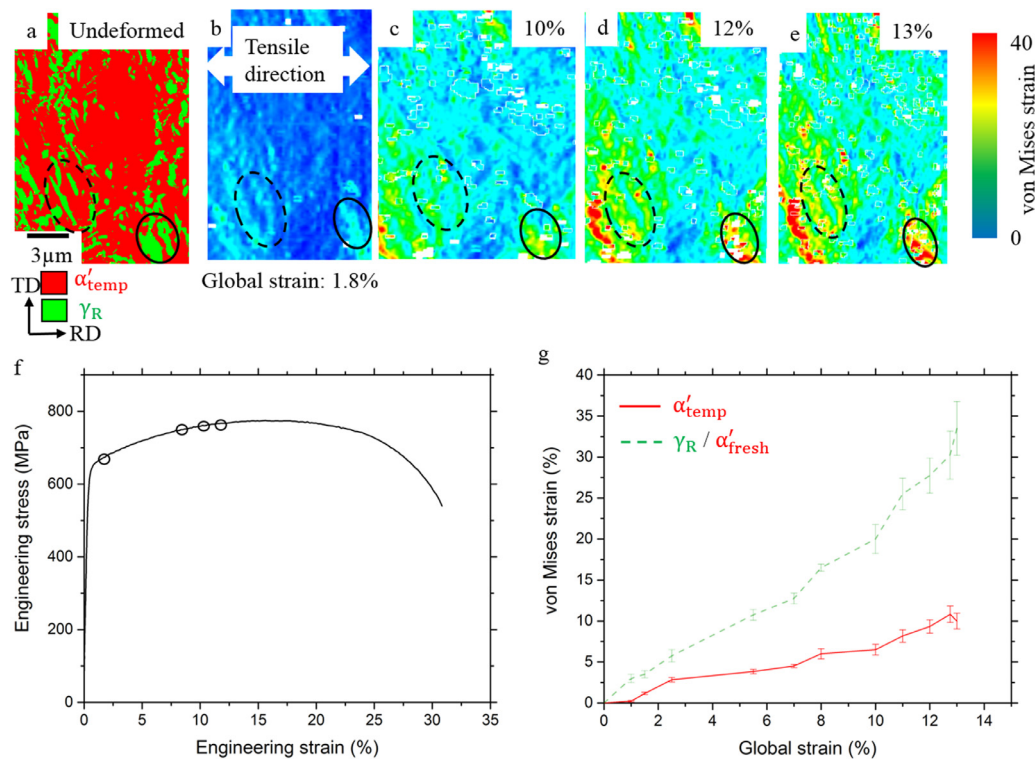
Fig. 8. (a) Phase maps of γ_R and α'_{temp} in the CRA materials and corresponding strain maps at (b) 1.8%, (c) 10%, (d) 12% and (e) 13% global strain. The strain values are highlighted in the (f) stress strain curve. (g) Evolution of the von Mises strains in γ_R/α'_{fresh} and α'_{temp} with increasing global strain. γ_R: reverted austenite; α'_{temp}: tempered martensite; α'_{fresh}: fresh martensite, i.e. newly transformed martensite; CRA: cold rolled and intercritically annealed.

nealing temperatures, has been attributed to the increased mobile dislocation density in the ferrite matrix due to the back transformation of γ_R to α'_{fresh} [2,39,41,46]. This has been assumed to be due to the decreased chemical and thermal stability of γ_R at high intercritical annealing temperatures resulting in a volume change during quenching [2,39,41,46].

4.2. Strain partitioning and mechanical properties

4.2.1. Strain partitioning in hot and cold rolled material

It has been suggested in earlier studies that continuous yielding in hot rolled medium Mn steels is due to the simultaneous deformation of both, lamellar shaped γ_R and lath α'_{temp}, at the early stages of deformation due to the high dislocation density within the α'_{temp} grains [47]. On the other hand, neutron diffraction experiments on hot rolled medium Mn steel have shown that first the softer γ_R grains deform plastically followed by plastic deformation of both, α'_{temp} and γ_R [36]. It should be noted that the microstructure investigated in [36] consisted of coarse grained γ_R with an average grain size above 2 µm and an ultra-fine grained $\gamma_R + \alpha'_{temp}$ matrix with a γ_R grain size of 0.6 µm. Both, coarse grained γ_R as well as ultra-fine grained γ_R in the $\gamma_R + \alpha'_{temp}$ matrix, were assumed to show the same deformation behavior based on the diffraction data [36].

Here, we used in situ µ-DIC in conjunction with EBSD to identify the local von Mises strains of individual grains and its relationship to their crystallographic orientation, spatial alignment and morphology.

The in situ tensile tests of the HRA medium Mn steel samples shown in Fig. 4 clearly reveal a complex deformation behavior where the imposed strain is partitioned between the different phases. Fig. 4 clearly denotes higher local von Mises strain within the γ_R grains as seen from the local von Mises strain maps (b – e) and the corresponding EBSD map (a). Fig. 4(g) indicates that $\gamma_R / \alpha'_{fresh}$ shows a high von Mises strain of 15% at a global strain of 7.1% while the α'_{temp} shows local von Mises strains well below 5% at the same global strain. Taking multiple sec-

tions across global strain maps such as presented in Fig. 4(g), the average local von Mises strain was calculated for each phase. Fig. 9(a) shows the local von Mises strain distribution within $\gamma_R / \alpha'_{fresh}$ and α'_{temp} versus the global strain for the HRA material deformed until necking. The results indicate that the local von Mises strain is concentrated in the soft γ_R islands in the early stages of yielding. The strain at higher global strains above 10% is accommodated by both, γ_R islands and α'_{temp} matrix. These results are in accordance with those reported for neutron diffraction experiments on similar medium Mn steels where yielding was a result of the softer austenite grains deforming plastically while the third stage resulted in the austenite and ferrite to deform plastically [36]. The ability of γ_R to accumulate dislocations or deform via the TWIP or TRIP mechanism results in the observed fast strain hardening during the early stages of deformation also causing continuous yielding. Apart from strain partitioning observed earlier through high resolution x-ray or neutron diffraction experiments [14,36], µ-DIC helps to locally resolve the concept of strain localization.

Fig. 9(b) shows the local von Mises strain distribution within $\gamma_R / \alpha'_{fresh}$ and α'_{temp} versus the global strain of the CRA material deformed until necking. Strain partitioning to the soft γ_R in the early stages of deformation is evident from Fig. 9(b). The local von Mises strain within the $\gamma_R / \alpha'_{fresh}$ is observed to be above 10% at a global strain of 5% while the local von Mises strain is well below 5% within the α'_{temp} at the same global strain. The local von Mises strain in the α'_{temp} increases above a global strain of 5%. The strain in γ_R results from dislocation slip and twining on the one hand, but also from shape distortion due to the transformation from γ_R to α'_{fresh}. Such shape change induced strains as a result of a martensitic phase transformation has been calculated earlier using the crystallographic theory of martensite [48–53]. For the present case (CRA material), in situ XRD measurements presented in Fig. 3(a) show no reduction in the volume fraction of γ_R until a global engineering strain of 10% (corresponding to 18% local von Mises strain in the $\gamma_R / \alpha'_{fresh}$ grains measured by µ-DIC). It is therefore assumed that
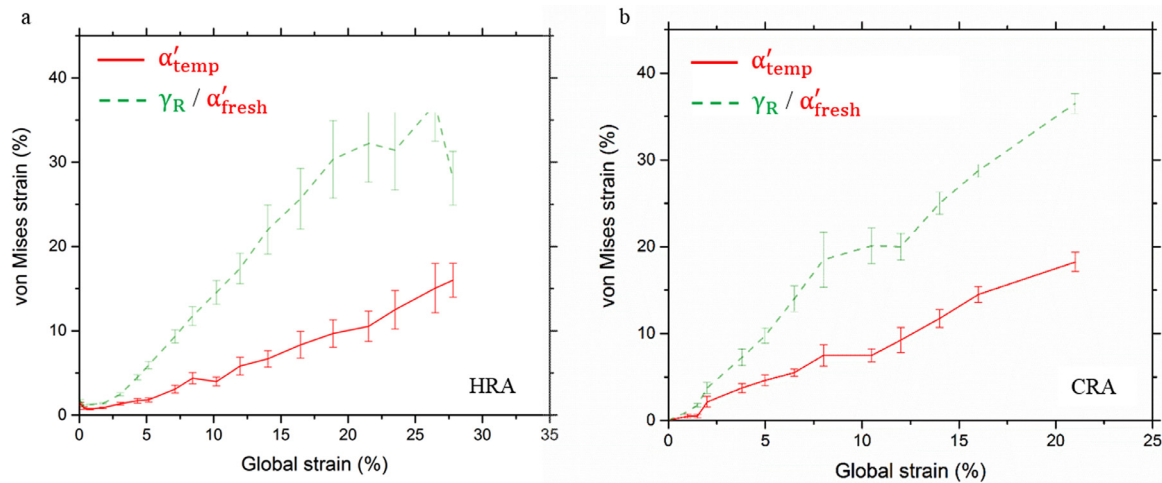
Fig. 9. Evolution of the von Mises strains in γ_R/α'_{fresh} and α'_{temp} with increasing global strain until necking in the (a) HRA and (b) CRA material. γ_R: reverted austenite; α'_{temp}: tempered martensite; α'_{fresh}: fresh martensite, i.e. newly transformed martensite; HRA: hot rolled and intercritically annealed; CRA: cold rolled and intercritically annealed.

the strain within the γ_R is not dominated by martensitic transformation induced shape changes but originates primarily from dislocation slip in the γ_R until a global strain of 10%.

It was predicted that when an austenitic specimen is assumed to transform completely into martensite, the associated maximum tensile elongation as a result of phase transformation would amount to 15% [54]. Consequently, when the austenite fraction amounts to 15%, the contribution of the martensitic transformation to elongation is only about 2.25% [54]. In the present case the austenite volume fraction amounts to 26% and 36% for CRA and HRA, respectively, and about 40% of the γ_R transforms to martensite, therefore the contribution to the global strain would be less than 3%. Hence, it is assumed that the high local von Mises strains in $\gamma_R / \alpha'_{fresh}$ are not dominated by shape change induced strain.

Microstructure-based finite element (FE) modeling of cold rolled medium Mn steel has predicted an intersection of the flow stress curves of the individual phases [15]. The flow stresses of the γ_R were calculated to be lower than that of α'_{temp} in the early stages of yielding [15]. Above an engineering strain of 10%, due to deformation twinning or strain induced martensitic transforming in the γ_R, flow stresses of γ_R were higher than that of α'_{temp} causing a crossover of the flow stress curves of the individual phases [15]. Such a crossover of the strain contributions of the individual phases is not observed in the present HRA and CRA samples, Fig. 9.

Strain localization in hot rolled material

Role of austenite spatial alignment and crystallography

Fig. 5 shows a larger area of the HRA material where strain localization in clusters is evident. The γ_R deforms plastically at lower strains while the α'_{temp} deforms elastically followed by plastic deformation of both the phases as seen from Fig. 4 and from neutron diffraction experiments [36]. Apart from strain partitioning, the strain localization effect can be explained in terms of colonies of lamellar-like γ_R grains having the same spatial alignment and crystallographic orientation. Maximum geometrical shear is expected for lamellar-shaped γ_R grains which are at an angle of 45° towards the tensile direction and propagate at an angle of 45° into the sample. This geometrical shear is independent of the crystallography-dependent resolved shear stresses on the different crystallographic planes [55]. Due to the K-S orientation relationship with the neighboring α'_{temp} matrix, a {111} plane is always aligned along the lamella's larger dimension. This sort of morphological-geometrically induced strain localization is seen in Fig. 6(d) within areas $1_{HRA\ Fig.\ 6}$ and $3_{HRA\ Fig.\ 6}$. Specifically, the observed strain localization occurs in pack-

ets of single prior austenite grains where the γ_R colonies have the same crystallographic orientation and spatial alignments.

A memory effect causing that austenite formed during reversion annealing has the same crystallographic orientation of the prior austenite grains has been observed before and attributed to the presence of internal stresses in the martensite [35]. Hence, the Schmid factors and Taylor factors are the same for γ_R colonies with the same crystallographic orientations in a prior austenite grain. Therefore, a merely crystallographic analysis does not provide sufficient information regarding the observed strain localization effects. Similarly, relaxed constraints models used in earlier studies for predicting rolling textures in polycrystalline FCC metals consider the spatial alignment of pancake shaped grains [56,57]. As the γ_R can be considered as lamellar-shaped grains, the shear incompatibility of them to the neighboring α'_{temp} matrix is assumed to decrease with decreasing thickness to length and/or width ratio [56]. Shearing of a lamellar-shaped grain along its length results in a rapid increase in shear incompatibility with increasing strain with respect to the neighboring matrix.

Earlier, single through-thickness block boundaries in lath martensite oriented 45° to the loading axis have shown easy glide along the lath boundaries [58], which might be due to retained austenite films at the lath boundaries in low carbon martensitic steels [59]. The importance of the spatial alignment of grains have been observed also in γ-TiAl alloys and in pearlitic steels [60,61]. Specifically, strain localization in the lamellar γ phase of γ-TiAl aligned approximately 45° to the loading axis was observed using DIC [60,62]. Micro-compression tests on pearlitic steels have shown similar strain localization in the ferrite where the interlamellar spacing and their orientation to the loading axis had significant effects on the hardening capacity [61]. The difference to the present study on medium manganese steels is the TRIP effect causing the softer γ_R phase to transform to α'_{fresh} during deformation.

Recently, differences in strain accommodation of globular and lath shaped γ_R were observed in a medium Mn steel resulting in different yielding behaviors of cold and hot rolled materials [63]. A two-step annealing treatment was applied to obtain a lath shaped morphology of γ_R [63] which is similar to the hot rolled microstructure observed in the present study, yet, with a smaller prior austenite grain size. The mechanical stabilization of γ_R based on the morphology was used to differentiate between different types of γ_R [63].

In HRA medium Mn steels, γ_R is formed between the lath boundaries. Within a specific packet of α' in a prior austenite grain, the γ_R has the same spatial alignment as well as the same crystallographic orientation, see Fig. 2(a) and Supplementary Movie 1. Other packets within the same
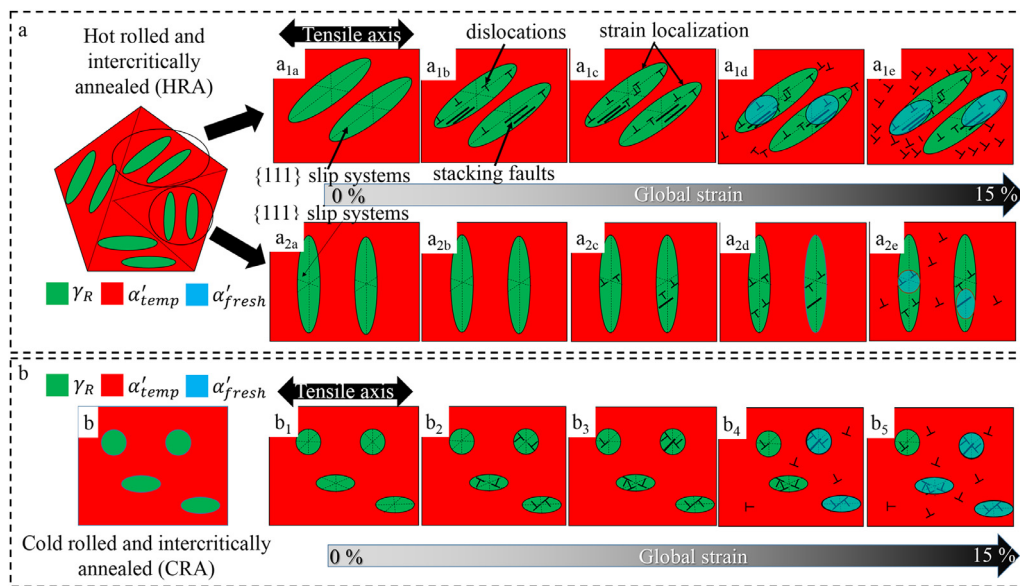
Fig. 10. Schematic sketch of the spatial alignment dependent deformation and transformation behaviors in (a_1 and a_2) HRA and (b) CRA material. . γ_R: reverted austenite; α'_{temp}: tempered martensite; α'_{fresh}: fresh martensite, i.e. newly transformed martensite; HRA: hot rolled and intercritically annealed; CRA: cold rolled and intercritically annealed.

prior austenite grain may have the same crystallographic orientation but different spatial alignments. Therefore, colonies of γ_R islands with the same spatial alignment and crystallographic orientation can be considered to be plastically acting like one large γ_R grain resulting in yielding. If the spatial alignment of such a cluster of γ_R islands is ideally orientated for shear, strain localization within these γ_R island colonies occurs as depicted in the schematic drawing in Fig. 10 (a_{1a-e}), hence, resulting in faster transformation to α'_{fresh}. Other clusters of γ_R islands within the same prior austenite grain which exhibit a different spatial alignment towards the loading direction show less intense strain localization, Fig. 10 (a_{2a-e}), and a lower transformation rate to α'_{fresh}. Such localization effects can be clearly seen in Case 1 in Fig. 6(d) and Supplementary Fig. 1. It has been reported that during deformation of medium Mn steels the TRIP or TWIP+TRIP mechanisms occur, whereby α'_{fresh} is formed both by shearing of ε-martensite variants at their intersections [64] and at twin intersections [65,66]. Both mechanisms, TRIP and TWIP, result from the dissociation of dislocations and from the strain-induced formation of extended stacking faults. The ECCI images shown for areas $1_{HRA\ Fig.\ 6}$ and $2_{HRA\ Fig.\ 6}$, (Fig. 6), show a dense deformation structure with multiple slip systems activated in area $1_{HRA\ Fig.\ 6}$, while area $2_{HRA\ Fig.\ 6}$ exhibits only one activated slip system with a lower density of stacking faults. To understand the role of the activation of slip systems based on the spatial alignment of γ_R at lower deformation conditions, Fig. 11 shows two different areas of an HRA sample at 5% global strain. Fig. 11(a) and (b) present phase and IPF maps of the two areas $1_{HRA\ Fig.\ 11}$ and $2_{HRA\ Fig.\ 11}$ with different γ_R lamellar loading angles (c). Fig. 11(d) and (e) show KAM maps of γ_R and $\alpha'_{temp} + \alpha'_{fresh}$ at 5% global strain while (f) and (g) are ECCI images of areas $1_{HRA\ Fig.\ 11}$ and $2_{HRA\ Fig.\ 11}$. Fig. 11(h) shows the corresponding Thompson tetrahedron for the γ_R revealing the slip systems and slip traces of {111} planes together with their respective Schmid factors for uniaxial stress. The γ_R and $\alpha'_{temp} + \alpha'_{fresh}$ KAM maps show higher values in area $1_{HRA\ Fig.\ 11}$ than in area $2_{HRA\ Fig.\ 11}$, indicating higher strain in area $1_{HRA\ Fig.\ 11}$ where both phases are spatially aligned by 45° to the tensile axis. Stacking faults in the γ_R are highlighted by the white arrows in the ECCI images. Area $2_{HRA\ Fig.\ 11}$ in Fig. 11(g) has a single crystallographic variant of stacking faults. These faults are on the $(1\bar{1}1)$ plane having the highest Schmid factor of 0.48 for 1/2[011] perfect dislocations. The corresponding partial dislocations have Schmid factors of 0.47 and 0.36 for 1/6[121] and 1/6[21$\bar{1}$] directions, respectively. In area $1_{HRA\ Fig.\ 11}$, stacking faults

on the $(1\bar{1}1)$ plane which has the highest Schmid factor are observed as shown by the white arrow, Fig. 11(f). In area $1_{Figure\ 11}$, the $(1\bar{1}1)$ plane lies along the lamellar length. In addition to stacking faults on the $(1\bar{1}1)$ plane, other stacking fault systems are also observed. However, the density of stacking faults along the lamellar length is higher than along the other directions. This effect is attributed to (partial) dislocation pile-ups at the ends of the lamellae and at the boundaries, Fig. 10 (a_{1b}). Similar observations were made in Case 1, Fig. 6(h) and (i), shown as enlarged images in the Supplementary Fig. 3. The activation of multiple slip systems in FCC metals promotes formation of high accumulated forest dislocation density values through dislocation-dislocation interactions and formation of sessile junctions [67,68]. Accordingly, increased strain hardening during the early stages of deformation has been attributed to the increase in forest dislocation densities [67,68]. Similarly, the nucleation of bcc martensite at the intersection of two stacking faults on two {111} planes were proposed using the Bogers-Burgers and the Olson-Cohen models [69,70]. Recently, molecular dynamics simulations have also described the nucleation of bcc martensite based on intersections of stacking faults [71]. Multiple variants of stacking faults observed in deformed γ_R areas $1_{HRA\ Fig.\ 6}$ and $3_{HRA\ Fig.\ 6}$ in Case 1 (Fig. 6) and area $1_{HRA\ Fig.\ 11}$ (Fig. 11) are therefore assumed to promote the transformation of γ_R to α'_{fresh} during deformation. Thus deformation behavior in lamellar shaped grains is dependent on its spatial alignment since the grain size effect may be misleading due to its morphology and viewing plane.

Role of the martensite crystallography and spatial alignment

Fig. 9(a) reveals that the local von Mises strain of α'_{temp} is below 5% at global strains of 10%. It is assumed that strain localization in α'_{temp} is dependent on the crystallography and spatial alignment, similar to γ_R. A similar strain localization dependence has been reported for low carbon lath martensite showing that dislocation slip is controlled by the morphological and crystallographic constraints [72]. In-lath-plane slip systems were reported to be responsible for enhanced local plasticity of lath martensite due to the long mean free path in this direction [73–75].

In Case 1 no difference in the strain localization behavior is observed for areas $1_{HRA\ Fig.\ 6}$ and $3_{HRA\ Fig.\ 6}$, even though the colony of γ_R is surrounded by α'_{temp} with different crystallographic orientations, Fig. 6. This is assumed to be due to similar spatial alignments and sim-
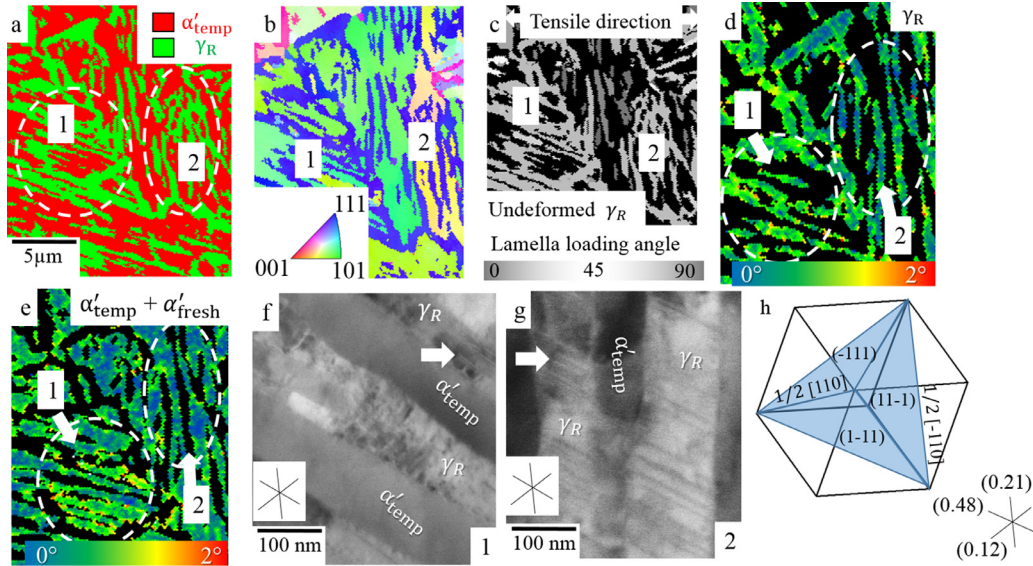
Fig. 11. (a) Phase, (b) IPF and (c) lamellar loading angle maps of undeformed HRA sample after intercritical annealing. KAM maps of 5% global strain (d) and (e). ECCI images of (f) area $1_{\text{HRA Fig. 11}}$ and (g) area $2_{\text{HRA Fig. 11}}$ along with (h) the corresponding Thompson tetrahedral showing the slip systems and the calculated Schmid factors for perfect dislocations assuming a uniaxial stress state. : reverted austenite; : tempered martensite; : fresh martensite, i.e. newly transformed martensite; HRA : hot rolled and intercritically annealed.

ilar Schmid factors for {110} <111> slip in α'_{temp} for both orientations. The transfer of strain from γ_R to α'_{temp} is therefore dependent on the extent of strain and the spatial alignment of the γ_R colony within it. This is seen in the KAM map of HRA $\alpha'_{\text{temp}} + \alpha'_{\text{fresh}}$ at 5% global strain in Fig. 11(e). The KAM values of $\alpha'_{\text{temp}} + \alpha'_{\text{fresh}}$ in area $1_{\text{HRA Fig. 11}}$ surrounding the highly strained γ_R colony in Fig. 11(d) are higher than those of area $2_{\text{HRA Fig. 11}}$ where the γ_R is less deformed.

Strain localization within a colony of γ_R not spatially aligned for pure shear with a hard orientation, is also dependent on the crystallographic orientation of the α'_{temp} matrix around it as can be seen in Case 2, Fig. 7. The γ_R in area $1_{\text{HRA Fig. 7}}$ and $2_{\text{HRA Fig. 7}}$ has the same spatial alignment and crystallographic orientation, Fig. 7(b). The only difference of these two areas is the crystallographic orientation of the adjacent α'_{temp}, Fig. 7(a), resulting in different Schmid factors for slip in α'_{temp} (Fig. 7(c)). Consequently it is assumed that the α'_{temp} induces a shielding effect on the γ_R which is higher if the α'_{temp} has a lower Schmid factor for dislocation slip. Hence, the strain is assumed to be accommodated by both, γ_R and α'_{temp}, at high global strains and strain localization is controlled by the crystallographic orientation of the α'_{temp}.

4.2.2. Strain partitioning and strain localization in hot rolled vs. cold rolled material

Both, HRA and CRA medium Mn steel show pronounced strain partitioning resulting in higher local von Mises strain in γ_R at the early stages of deformation (i.e., below 5%). In both conditions this is due to the fact that at the low intercritical annealing temperature of 555 °C no martensite recrystallization occurs. This results in initially lower flow stresses of γ_R than of α'_{temp}. The main difference between the HRA and CRA material is the γ_R micro-texture, as discussed in the following.

Strain localization is observed in the HRA samples. Colonies of γ_R lamellar with the same crystallographic orientation and spatial alignment towards the tensile axis appear to behave like a single large γ_R unit. The size of this colony is determined by the martensite packet size. This is especially important for yielding and results in a lower yield stress of the HRA material. In comparison, the γ_R grains in the CRA samples are strained more homogeneously. This clustered localization effect in the HRA samples causes an earlier onset of the TRIP effect in the strain-localized regions as shown by the schematic in Fig. 10 (a_{1d-e}).

Post deformation EBSD maps presented in Fig. 6(f) show a 35% reduction in area fraction of γ_R in areas $1_{\text{HRA Fig. 6}}$ and $3_{\text{HRA Fig. 6}}$. The areas with higher γ_R area fraction reduction correspond to γ_R colonies with higher von Mises strains as also seen in Supplementary figure 1. This effect is assumed to be due to increasing relative γ_R grain sizes, where γ_R colonies of similar crystallographic orientation and spatial alignment act like a larger γ_R grain. The random distribution of different γ_R K-S variants in the CRA samples results in each grain being strained individually according to its crystallographic orientation, causing less strain localization. The observed differences in the yield stresses of the HRA and the CRA material (Fig. 2) are assumed to be partly due to this relative grain size effect as shown by the schematic in Fig. 10. It should be noted that this effect applies only when the γ_R shows a higher von Mises strain in the early stages of deformation when compared to the α'_{temp} matrix for both, the HRA and CRA materials. Due to the observed strain localization in γ_R clusters in the HRA samples, it is assumed that strain-induced transformation to α'_{fresh} starts already at smaller loads than in the HRA samples which is also observed in Fig. 3(a) from the in situ XRD data. This results in different mechanical stabilities of the γ_R grains in the HRA sample as compared to the CRA sample. Thus a less pronounced yielding is observed in the HRA specimens relative to the CRA material.

Fig. 12(a) shows a $\ln(f_{\gamma 0}) - \ln(f_{\gamma})$ vs. true strain plot comparing the apparent mechanical stability of γ_R for the HRA and CRA samples. The apparent mechanical stability factor (k) of γ_R is quantified using the following equation [76]

$$f_{\gamma} = f_{\gamma 0} \exp(-k\varepsilon) \tag{1}$$

Here, f_{γ}, $f_{\gamma 0}$ and k are the initial γ_R fraction, the γ_R fraction at true strain ε, and the mechanical stability of γ_R, respectively. A higher value of k thus represents a higher driving force for the $\gamma_R \rightarrow \alpha'_{\text{fresh}}$ transformation. The CRA sample has a higher k value of 9.36 as compared to the HRA sample, which has a value of 3.45. Thus, using Eq. (1), the apparent mechanical stability factor, k, illustrates that γ_R is less stable at lower strains in the HRA material than in the CRA material due to the localization of strain in HRA. The offset differences in the true strain between the HRA and CRA samples causes the slope of mechanical stability to not to pass through the origin due to the differences in $\gamma_R \rightarrow \alpha'_{\text{fresh}}$ transformation rates. Yet, it should be noted here, that the apparent
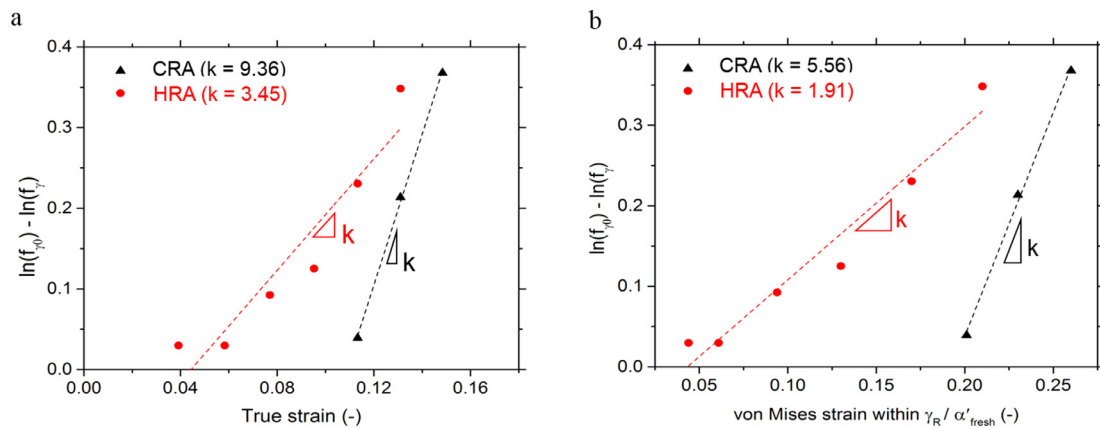
Fig. 12. (a) $\ln(f_{\gamma 0}) - \ln(f_{\gamma})$ vs true strain plot for γ_R apparent mechanical stability values of HRA and CRA samples. (b) $\ln(f_{\gamma 0}) - \ln(f_{\gamma})$ vs. the von Mises strain within $\gamma_R / \alpha'_{fresh}$ for the HRA and CRA samples along with the γ_R mechanical stability factor (k). γ_R: reverted austenite; α'_{fresh}: fresh martensite, i.e. newly transformed martensite; HRA: hot rolled and intercritically annealed; CRA: cold rolled and intercritically annealed.

mechanical stability of γ_R - when calculated for the global strain - can be different from the actual local γ_R strain within the grains in a multiphase system. Hence, the apparent mechanical stability factor k of γ_R, when plotted against the global strain value, could provide misleading information on its true micromechanical response.

Fig. 12(b) presents a $\ln(f_{\gamma 0}) - \ln(f_{\gamma})$ vs. the von Mises strain plot for $\gamma_R / \alpha'_{fresh}$ in the HRA and CRA samples together with the corresponding γ_R mechanical stability factor (k). Differences between the mechanical stability of γ_R when plotted against the global strain or the von Mises strain within $\gamma_R / \alpha'_{fresh}$ are quite apparent as the k value reduces from 9.36 to 5.56 and from 3.45 to 1.91 for the CRA and HRA samples, respectively. Thus the onset of the TRIP effect in the γ_R gives a more precise value when plotted against the von Mises strain within γ_R and α'_{fresh} than when plotted against the global strain although the real mechanical stability may change within different colonies of γ_R due to the strain localization effect. The offset for the slopes in Fig. 12 are due to the change in γ_R fraction at higher global strains.

The present in situ μ-DIC study shows that in addition to spectral and hydrostatic effects [77], the spatial alignment of lamellar γ_R colonies towards the tensile loading direction affects the deformation and strain localization behavior. Hence, it should be considered when tailoring the mechanical properties of medium Mn steels using heat treatments. γ_R colonies of similar crystallographic orientations and spatial alignment result in early stage strain localization in HRA medium Mn steel. These colonies act like single larger γ_R grains when compared to grains in CRA material where the strain distribution is more homogenous due to the random distribution of K-S variants leading to higher yield stresses.

5. Medium Mn steel design criteria

5.1. Hot rolled material

Previous studies have already reported the dependence of the tensile behavior of hot rolled medium Mn steel on the intercritical annealing temperature and time [38,78,79]. Austenitization after cold rolling produces a microstructure similar to that of hot rolled samples. The results presented above reveal that the prior austenite texture memory effect of γ_R and its spatial alignments are controlling factors influencing the tensile behavior. Since localization of strain is seen within colonies of γ_R having the same crystallographic orientation and spatial alignment, the following design criteria are suggested for improving the material's properties by adjusting specific process parameters without changing its composition.

- Prior austenite grain size: One way of increasing the yield stress lies in reducing the strain localization areas as observed in Fig. 6. The size of colonies of similar spatially aligned γ_R are dependent on

the martensite packet size within the prior austenite grain. Reducing the prior austenite grain size would thus reduce the resulting martensite packet size [74,80]. This would in turn reduce the size of colonies with similar spatially aligned and crystallographically oriented γ_R. As a result, this approach should help reducing zones of premature strain localization, thus increasing the yield stress.
- Crystallographic texture: The texture memory effect of the γ_R grains inside the prior austenite grain plays an important role in controlling strain hardening. Breaking the texture memory effect of the γ_R inside the prior austenite grain, rendering it closer to the texture spread observed in the cold rolled material, would increase the strain hardenability of the hot rolled sample.

5.2. Cold rolled material

The intercritical annealing temperature and holding times for cold rolled medium Mn steel are critical factors influencing Lüders band propagation and elongation [37,39–42,46]. Approaches for eliminating Lüders bands have been to intercritically anneal the material at high intercritical annealing temperatures where the γ_R is thermally less stable resulting in back transformation to α'_{fresh} during the quenching stage [2,39,41,46]. Such treatment would result in loss of ductility though. Intercritically annealing the material at low temperatures prevents equiaxed ferrite formation by martensite recrystallization. Increased holding time results in an increase in γ_R volume fraction until compositional partition and volume fraction equilibrium stages are obtained. As observed from Fig. 8, when a sufficiently large volume fraction of γ_R is present, the flow stresses of γ_R is lower than that of α'_{temp} resulting in continuous yielding and sufficient strain hardening.

6. Conclusions

1. Designing medium Mn steels by selecting low intercritical annealing temperatures and long holding times results in avoiding recrystallization of α'_{temp} and an increased fraction of γ_R. This prevents macroscopical localization of strain in ferrite which would form during recrystallization of α'_{temp} and would promote the formation of Lüders bands and thus of a pronounced yield point. Increased holding times result in a sufficiently increased volume fraction of γ_R in order to prevent strain localization within the recovered α'_{temp} grains.
2. In the present study continuous yielding and higher local von Mises strain in γ_R than in α'_{temp} were observed in both, the hot rolled and cold rolled intercritically annealed material. Strain is taken up by $\gamma_R / \alpha'_{fresh}$ and α'_{temp} at global strains beyond 10% in hot rolled and 5% in cold rolled samples. The strain within the γ_R is not entirely contributed from shape strain distortion.

3. The lamellar morphology of γ_R in hot rolled and intercritically annealed sample makes it difficult to understand the grain size effect on deformation due to the spatial alignment effect as seen on a sample surface.

4. Apart from strain partitioning, strain localization was observed in hot rolled medium Mn steel samples. Colonies of lamellar γ_R islands inclined 45° to the loading axis and a lamella normal at 45° to ND, tend to experience maximum geometrical shear and accommodate the highest local von Mises strains. Similar crystallographically oriented γ_R colonies within the same prior austenite grain inclined at not 45° to the loading axis experience less geometrical shear and less local von Mises strain. This results in strain localization within colonies of γ_R islands. Strain localization leads to faster strain induced martensitic transformation of γ_R to α'_{fresh}, resulting in different apparent γ_R mechanical stabilities and also faster transfer of strain to α'_{temp} next to it. This localization within a colony is interpreted such that the colony acts like one large γ_R grain, i.e. like an increase in the effective grain size. The α'_{temp} crystallography plays an important role in determining the extent to which strain is partitioned, particularly for γ_R deformation which are not spatially aligned for shear at higher global strains.

5. Strain is more homogeneously partitioned within the γ_R islands in the cold rolled medium Mn steel. This is due to the random distribution of K-S variants as the prior austenite grains had been plastically broken up during cold rolling prior to intercritical annealing.

6. The relative grain size effect in hot rolled samples is assumed to cause the observed lower yield stresses in hot rolled samples compared to the cold rolled samples in cases where both show continuous yielding.

Acknowledgements

Supplementary material

Supplementary material associated with this article can be found, in the online version, at doi:10.1016/j.mtla.2019.100252.

References

[1] C. Wang, W. Cao, J. Shi, C. Huang, H. Dong, Deformation microstructures and strengthening mechanisms of an ultrafine grained duplex medium-Mn steel, Mater. Sci. Eng. A. 562 (2013) 89–95, doi:10.1016/j.msea.2012.11.044.

[2] S. Lee, B.C.D. Cooman, On the selection of the optimal intercritical annealing temperature for medium Mn TRIP steel, Metall. Mater. Trans. A. 44 (2013) 5018–5024, doi:10.1007/s11661-013-1860-2.

[3] R. Zhang, W.Q. Cao, Z.J. Peng, J. Shi, H. Dong, C.X. Huang, Intercritical rolling induced ultrafine microstructure and excellent mechanical properties of the medium-Mn steel, Mater. Sci. Eng. A. 583 (2013) 84–88, doi:10.1016/j.msea.2013.06.067.

[4] Y.-K. Lee, J. Han, Current opinion in medium manganese steel, Mater. Sci. Technol. 31 (2014) 843–856, doi:10.1179/1743284714y.0000000722.

[5] C.-Y. Lee, J. Jeong, J. Han, S.-J. Lee, S. Lee, Y.-K. Lee, Coupled strengthening in a medium manganese lightweight steel with an inhomogeneously grained structure of austenite, Acta Mater 84 (2015) 1–8, doi:10.1016/j.actamat.2014.10.032.

[6] X. Zhao, Y. Shen, L. Qiu, Y. Liu, X. Sun, L. Zuo, Effects of intercritical annealing temperature on mechanical properties of Fe-7.9Mn-0.14Si-0.05Al-0.07C Steel, Materials 7 (2014) 7891–7906, doi:10.3390/ma7127891.

[7] E.J. Seo, L. Cho, B.C.D. Cooman, Application of quenching and partitioning processing to medium Mn steel, Metall. Mater. Trans. A. 46 (2015) 27–31, doi:10.1007/s11661-014-2657-7.

[8] S. Lee, S.-J. Lee, B.C. De Cooman, Austenite stability of ultrafine-grained transformation-induced plasticity steel with Mn partitioning, Scr. Mater. 65 (2011) 225–228, doi:10.1016/j.scriptamat.2011.04.010.

[9] O. Dmitrieva, D. Ponge, G. Inden, J. Millán, P. Choi, J. Sietsma, D. Raabe, Chemical gradients across phase boundaries between martensite and austenite in steel studied by atom probe tomography and simulation, Acta Mater 59 (2011) 364–374, doi:10.1016/j.actamat.2010.09.042.

[10] J.H. Ryu, D.-I. Kim, H.S. Kim, H.K.D.H. Bhadeshia, D.-W. Suh, Strain partitioning and mechanical stability of retained austenite, Scr. Mater. 63 (2010) 297–299, doi:10.1016/j.scriptamat.2010.04.020.

[11] C.C. Tasan, M. Diehl, D. Yan, M. Bechtold, F. Roters, L. Schemmann, C. Zheng, N. Peranio, D. Ponge, M. Koyama, K. Tsuzaki, D. Raabe, An overview of dual-phase steels: advances in microstructure-oriented processing and micromechanically guided design, Annu. Rev. Mater. Res. 45 (2015) 391–431, doi:10.1146/annurev–matsci-070214-021103.

[12] C.C. Tasan, M. Diehl, D. Yan, C. Zambaldi, P. Shanthraj, F. Roters, D. Raabe, Integrated experimental–simulation analysis of stress and strain partitioning in multiphase alloys, Acta Mater 81 (2014) 386–400, doi:10.1016/j.actamat.2014.07.071.

[13] M.-M. Wang, C.C. Tasan, D. Ponge, A. Kostka, D. Raabe, Smaller is less stable: size effects on twinning vs. transformation of reverted austenite in TRIP-maraging steels, Acta Mater 79 (2014) 268–281, doi:10.1016/j.actamat.2014.07.020.

[14] P.J. Gibbs, B.C. De Cooman, D.W. Brown, B. Clausen, J.G. Schroth, M.J. Merwin, D.K. Matlock, Strain partitioning in ultra-fine grained medium-manganese transformation induced plasticity steel, Mater. Sci. Eng. A. 609 (2014) 323–333, doi:10.1016/j.msea.2014.03.120.

[15] M.I. Latypov, S. Shin, B.C. De Cooman, H.S. Kim, Micromechanical finite element analysis of strain partitioning in multiphase medium manganese TWIP+TRIP steel, Acta Mater 108 (2016) 219–228, doi:10.1016/j.actamat.2016.02.001.

[16] S.L. Wong, M. Madivala, U. Prahl, F. Roters, D. Raabe, A crystal plasticity model for twinning- and transformation-induced plasticity, Acta Mater 118 (2016) 140–151, doi:10.1016/j.actamat.2016.07.032.

[17] C.C. Tasan, J.P.M. Hoefnagels, M.G.D. Geers, Microstructural banding effects clarified through micrographic digital image correlation, Scr. Mater. 62 (2010) 835–838, doi:10.1016/j.scriptamat.2010.02.014.

[18] D. Yan, C.C. Tasan, D. Raabe, High resolution in situ mapping of microstrain and microstructure evolution reveals damage resistance criteria in dual phase steels, Acta Mater 96 (2015) 399–409, doi:10.1016/j.actamat.2015.05.038.

[19] L. Allais, M. Bornert, T. Bretheau, D. Caldemaison, Experimental characterization of the local strain field in a heterogeneous elastoplastic material, Acta Metall. Mater. 42 (1994) 3865–3880, doi:10.1016/0956-7151(94)90452-9.

[20] D.T. Pierce, J.A. Jiménez, J. Bentley, D. Raabe, J.E. Wittig, The influence of stacking fault energy on the microstructural and strain-hardening evolution of Fe–Mn–Al–Si steels during tensile deformation, Acta Mater 100 (2015) 178–190, doi:10.1016/j.actamat.2015.08.030.

[21] A. Saeed-Akbari, J. Imlau, U. Prahl, W. Bleck, Derivation and variation in composition-dependent stacking fault energy maps based on subregular solution model in high-manganese steels, Metall. Mater. Trans. A. 40 (2009) 3076–3090, doi:10.1007/s11661-009-0050-8.

[22] D.P. Koistinen, R.E. Marburger, A general equation prescribing the extent of the austenite-martensite transformation in pure iron-carbon alloys and plain carbon steels, Acta Metall 7 (1959) 59–60, doi:10.1016/0001-6160(59)90170-1.

[23] C.C. Tasan, J.P.M. Hoefnagels, M. Diehl, D. Yan, F. Roters, D. Raabe, Strain localization and damage in dual phase steels investigated by coupled in-situ deformation experiments and crystal plasticity simulations, Int. J. Plast. 63 (2014) 198–210, doi:10.1016/j.ijplas.2014.06.004.

[24] S.-H. Joo, J.K. Lee, J.-M. Koo, S. Lee, D.-W. Suh, H.S. Kim, Method for measuring nanoscale local strain in a dual phase steel using digital image correlation with nanodot patterns, Scr. Mater. 68 (2013) 245–248, doi:10.1016/j.scriptamat.2012.10.025.

[25] M. Krottenthaler, C. Schmid, J. Schaufler, K. Durst, M. Göken, A simple method for residual stress measurements in thin films by means of focused ion beam milling and digital image correlation, Surf. Coat. Technol. 215 (2013) 247–252, doi:10.1016/j.surfcoat.2012.08.095.

[26] M.D. McMurtrey, G.S. Was, B. Cui, I. Robertson, L. Smith, D. Farkas, Strain localization at dislocation channel–grain boundary intersections in irradiated stainless steel, Int. J. Plast. Complete (2014) 219–231, doi:10.1016/j.ijplas.2014.01.001.

[27] F.D. Gioacchino, J.Q. da Fonseca, Plastic strain mapping with sub-micron resolution using digital image correlation, Exp. Mech. 53 (2013) 743–754, doi:10.1007/s11340-012-9685-2.

[28] A. Orozco-Caballero, D. Lunt, J.D. Robson, J. Quinta da Fonseca, How magnesium accommodates local deformation incompatibility: a high-resolution digital image correlation study, Acta Mater. 133 (2017) 367–379, doi:10.1016/j.actamat.2017.05.040.

[29] Z. Zhao, M. Ramesh, D. Raabe, A.M. Cuitiño, R. Radovitzky, Investigation of three-dimensional aspects of grain-scale plastic surface deformation of an aluminum oligocrystal, Int. J. Plast. 24 (2008) 2278–2297, doi:10.1016/j.ijplas.2008.01.002.

[30] D. Raabe, M. Sachtleber, Z. Zhao, F. Roters, S. Zaefferer, Micromechanical and macromechanical effects in grain scale polycrystal plasticity experimentation and simulation, Acta Mater 49 (2001) 3433–3441, doi:10.1016/S1359-6454(01)00242-7.

[31] S. Zaefferer, S.I. Wright, D. Raabe, Three-dimensional orientation microscopy in a focused ion beam–scanning electron microscope: a new dimension of microstructure characterization, Metall. Mater. Trans. A. 39 (2008) 374–389, doi:10.1007/s11661-007-9418-9.

[32] G. Stechmann, S. Zaefferer, P. Konijnenberg, D. Raabe, C. Gretener, L. Kranz, J. Perrenoud, S. Buecheler, A.N. Tiwari, 3-Dimensional microstructural characterization of CdTe absorber layers from CdTe/CdS thin film solar cells, Sol. Energy Mater. Sol. Cells. 151 (2016) 66–80, doi:10.1016/j.solmat.2016.02.023.

[33] P.J. Konijnenberg, S. Zaefferer, S.B. Lee, A.D. Rollett, G.S. Rohrer, D. Raabe, Advanced methods and tools for reconstruction and analysis of grain boundaries from 3D-EBSD data sets, Mater. Sci. Forum. (2012), doi:10.4028/www.scientific.net/MSF.702-703.475.

[34] N. Nakada, R. Fukagawa, T. Tsuchiyama, S. Takaki, D. Ponge, D. Raabe, Inheritance of dislocations and crystallographic texture during martensitic reversion into austenite, ISIJ Int 53 (2013) 1286–1288, doi:10.2355/isijinternational.53.1286.

[35] N. Nakada, T. Tsuchiyama, S. Takaki, S. Hashizume, Variant selection of reversed austenite in lath martensite, ISIJ Int. 47 (2007) 1527–1532, doi:10.2355/isijinternational.47.1527.

[36] S. Lee, W Woo, B.C. de Cooman, Analysis of the tensile behavior of 12 pct Mn Multiphase ($\alpha + \gamma$) TWIP + TRIP steel by neutron diffraction, Metall. Mater. Trans. A. 47 (2016) 2125–2140, doi:10.1007/s11661-016-3407-9.

[37] J. Han, S.-J. Lee, C.-Y. Lee, S. Lee, S.Y. Jo, Y.-K. Lee, The size effect of initial martensite constituents on the microstructure and tensile properties of intercritically annealed Fe–9Mn–0.05C steel, Mater. Sci. Eng. A. 633 (2015) 9–16, doi:10.1016/j.msea.2015.02.075.

[38] G. Mishra, A.K. Chandan, S. Kundu, Hot rolled and cold rolled medium manganese steel: mechanical properties and microstructure, Mater. Sci. Eng. A. 701 (2017) 319–327, doi:10.1016/j.msea.2017.06.088.

[39] S. Lee, S.-J. Lee, S.S. Kumar, K. Lee, B.C.D. Cooman, Localized deformation in multiphase, ultra-fine-grained 6 Pct Mn transformation-induced plasticity steel, Metall. Mater. Trans. A. 42 (2011) 3638–3651, doi:10.1007/s11661-011-0636-9.

[40] J.H. Ryu, J.I. Kim, H.S. Kim, C.-S. Oh, H.K.D.H. Bhadeshia, D.-W. Suh, Austenite stability and heterogeneous deformation in fine-grained transformation-induced plasticity-assisted steel, Scr. Mater. 68 (2013) 933–936, doi:10.1016/j.scriptamat.2013.02.026.

[41] P.J. Gibbs, E.D. Moor, M.J. Merwin, B. Clausen, J.G. Speer, D.K. Matlock, Austenite stability effects on tensile behavior of manganese-enriched-austenite transformation-induced plasticity steel, Metall. Mater. Trans. A. 42 (2011) 3691–3702, doi:10.1007/s11661-011-0687-y.

[42] D.W. Suh, J.H. Ryu, M.S. Joo, H.S. Yang, K. Lee, H.K.D.H. Bhadeshia, Medium-alloy manganese-rich transformation-induced plasticity steels, Metall. Mater. Trans. A. 44 (2013) 286–293, doi:10.1007/s11661-012-1402-3.

[43] F.J. Humphreys, M. Hatherly, Chapter 14 - continuous recrystallization during and after large strain deformation, Recrystallization and Related Annealing Phenomena, Second Ed., Elsevier, Oxford, 2004, pp. 451–467, doi:10.1016/B978-008044164-1/50018-9.

[44] D.Z. Yang, E.L. Brown, D.K. Matlock, G. Krauss, Ferrite recrystallization and austenite formation in cold-rolled intercritically annealed steel, Metall. Trans. A. 16 (1985) 1385–1392, doi:10.1007/BF02658671.

[45] M. Haupt, A. Dutta, D. Ponge, S. Sandlöbes, M. Nellessen, G. Hirt, Influence of intercritical annealing on microstructure and mechanical properties of a medium manganese steel, in: Proceedings of the International Conference on the Technology of Plasticity, 2017.

[46] J.-M. Jang, S.-J. Kim, N.H. Kang, K.-M. Cho, D.-W. Suh, Effects of annealing conditions on microstructure and mechanical properties of low carbon, manganese transformation-induced plasticity steel, Met. Mater. Int. 15 (2009) 909–916, doi:10.1007/s12540-009-0909-7.

[47] J. Han, S.-J. Lee, J.-G. Jung, Y.-K. Lee, The effects of the initial martensite microstructure on the microstructure and tensile properties of intercritically annealed Fe–9Mn–0.05C steel, Acta Mater. 78 (2014) 369–377, doi:10.1016/j.actamat.2014.07.005.

[48] J.S. Bowles, J.K. Mackenzie, The crystallography of martensite transformations I, Acta Metall. 2 (1954) 129–137, doi:10.1016/0001-6160(54)90102-9.

[49] P.M. Kelly, Crystallography of lath martensite in steels, Mater. Trans. JIM. 33 (1992) 235–242, doi:10.2320/matertrans1989.33.235.

[50] M. Watanabe, C.M. Wayman, Crystallography of the martensite transformation in Fe–Al–C alloys, Metall. Mater. Trans. B. 2 (1971) 2229–2236, doi:10.1007/BF02917555.

[51] S. Morito, H. Tanaka, R. Konishi, T. Furuhara, T. Maki, The morphology and crystallography of lath martensite in Fe-C alloys, Acta Mater. 51 (2003) 1789–1799, doi:10.1016/S1359-6454(02)00577-3.

[52] C.M. Wayman, The phenomenological theory of martensite crystallography: interrelationships, Metall. Mater. Trans. A. 25 (1994) 1787–1795, doi:10.1007/BF02649029.

[53] S. Nambu, N. Shibata, M. Ojima, J. Inoue, T. Koseki, H.K.D.H. Bhadeshia, In situ observations and crystallographic analysis of martensitic transformation in steel, Acta Mater. 61 (2013) 4831–4839, doi:10.1016/j.actamat.2013.04.065.

[54] H.K.D.H. Bhadeshia, TRIP-assisted steels? ISIJ Int. 42 (2002) 1059–1060, doi:10.2355/isijinternational.42.1059.

[55] G.I. Taylor, Plastic strain in metals, Plast. Strain Met. (1938) 307–324.

[56] J. Hirsch, K. Lücke, Overview no. 76: mechanism of deformation and development of rolling textures in polycrystalline f.c.c. metals—II. Simulation and interpretation of experiments on the basis of Taylor-type theories, Acta Metall 36 (1988) 2883–2904, doi:10.1016/0001-6160(88)90173-3.

[57] H. Honneff, H. Mecking, A method for the determination of the active slip systems and orientation changes during single crystal deformation, in: Proceedings of the Textures of Materials, Berlin, 1978.

[58] J.P.M. Hoefnagels, C. Du, M.G.D. Geers, Boundary mechanics in lath martensite, studied by uni-axial micro-tensile tests, Micro Nanomechanics, 5, Springer, Cham, 2017, pp. 21–25, doi:10.1007/978-3-319-42228-2_4.

[59] S. Morito, K. Oh-ishi, K. Hono, T. Ohba, Carbon enrichment in retained austenite films in low carbon lath martensite steel, ISIJ Int. 51 (2011) 1200–1202, doi:10.2355/isijinternational.51.1200.

[60] C. Içöz, L. Patriarca, M. Filippini, S. Beretta, Strain accumulation in TiAl intermetallics via high-resolution digital image correlation (DIC), Proc. Eng. 74 (2014) 443–448, doi:10.1016/j.proeng.2014.06.295.

[61] M.W. Kapp, A. Hohenwarter, S. Wurster, B. Yang, R. Pippan, Anisotropic deformation characteristics of an ultrafine- and nanolamellar pearlitic steel, Acta Mater. 106 (2016) 239–248, doi:10.1016/j.actamat.2015.12.037.

[62] L. Patriarca, M. Filippini, S. Beretta, Digital image correlation-based analysis of strain accumulation on a duplex γ-TiAl, Intermetallics 75 (2016) 42–50, doi:10.1016/j.intermet.2016.05.013.

[63] K. Steineder, D. Krizan, R. Schneider, C. Béal, C. Sommitsch, On the microstructural characteristics influencing the yielding behavior of ultra-fine grained medium-Mn steels, Acta Mater. 139 (2017) 39–50, doi:10.1016/j.actamat.2017.07.056.

[64] B.C.D. Cooman, P. Gibbs, S. Lee, D.K. Matlock, Transmission electron microscopy analysis of yielding in ultrafine-grained medium Mn transformation-induced plasticity steel, Metall. Mater. Trans. A. 44 (2013) 2563–2572, doi:10.1007/s11661-013-1638-6.

[65] S. Lee, B.C.D. Cooman, Annealing temperature dependence of the tensile behavior of 10 pct Mn multi-phase TWIP-TRIP steel, Metall. Mater. Trans. A. 45 (2014) 6039–6052, doi:10.1007/s11661-014-2540-6.

[66] S. Lee, K. Lee, B.C.D. Cooman, Observation of the TWIP + TRIP plasticity-enhancement mechanism in Al-Added 6 Wt Pct medium Mn steel, Metall. Mater. Trans. A. 46 (2015) 2356–2363, doi:10.1007/s11661-015-2854-z.

[67] B. Devincre, L.P. Kubin, Simulations of forest interactions and strain hardening in FCC crystals, Model. Simul. Mater. Sci. Eng. 2 (1994) 559, doi:10.1088/0965-0393/2/3A/010.

[68] P. Hähner, A theory of dislocation cell formation based on stochastic dislocation dynamics, Acta Mater 44 (1996) 2345–2352, doi:10.1016/1359-6454(95)00364-9.

[69] A.J. Bogers, W.G. Burgers, Partial dislocations on the {110} planes in the B.C.C. lattice and the transition of the F.C.C. into the B.C.C. lattice, Acta Metall. 12 (1964) 255–261, doi:10.1016/0001-6160(64)90194-4.

[70] G.B. Olson, M. Cohen, A general mechanism of martensitic nucleation: part I. General concepts and the FCC $\rightarrow$ HCP transformation, Metall. Trans. A. 7 (1976) 1897–1904, doi:10.1007/BF02659822.

[71] S. Karewar, J. Sietsma, M.J. Santofimia, Effect of pre-existing defects in the parent fcc phase on atomistic mechanisms during the martensitic transformation in pure Fe: a molecular dynamics study, Acta Mater. 142 (2018) 71–81, doi:10.1016/j.actamat.2017.09.049.

[72] Y. Mine, K. Hirashita, H. Takashima, M. Matsuda, K. Takashima, Micro-tension behaviour of lath martensite structures of carbon steel, Mater. Sci. Eng. A. 560 (2013) 535–544, doi:10.1016/j.msea.2012.09.099.

[73] Measurement of Strain Distribution of Lath Martensite Microstructure during Tensile Deformation, (n.d.). https://www.jstage.jst.go.jp/article/jinstmet/73/9/73_9_720/_article (Accessed 13 April 2018).

[74] L. Morsdorf, O. Jeannin, D. Barbier, M. Mitsuhara, D. Raabe, C.C. Tasan, Multiple mechanisms of lath martensite plasticity, Acta Mater 121 (2016) 202–214, doi:10.1016/j.actamat.2016.09.006.

[75] A. Shibata, T. Nagoshi, M. Sone, S. Morito, Y. Higo, Evaluation of the block boundary and sub-block boundary strengths of ferrous lath martensite using a micro-bending test, Mater. Sci. Eng. A. 527 (2010) 7538–7544, doi:10.1016/j.msea.2010.08.026.

[76] K.-I. Sugimoto, M. Kobayashi, S.-I. Hashimoto, Ductility and strain-induced transformation in a high-strength transformation-induced plasticity-aided dual-phase steel, Metall. Trans. A. 23 (1992) 3085–3091, doi:10.1007/BF02646127.

[77] M.-M. Wang, C.C. Tasan, D. Ponge, D. Raabe, Spectral TRIP enables ductile 1.1 GPa martensite, Acta Mater 111 (2016) 262–272, doi:10.1016/j.actamat.2016.03.070.

[78] H. Luo, H. Dong, New ultrahigh-strength Mn-alloyed TRIP steels with improved formability manufactured by intercritical annealing, Mater. Sci. Eng. A. 626 (2015) 207–212, doi:10.1016/j.msea.2014.12.049.

[79] A. Arlazarov, M. Gouné, O. Bouaziz, A. Hazotte, G. Petitgand, P. Barges, Evolution of microstructure and mechanical properties of medium Mn steels during double annealing, Mater. Sci. Eng. A. 542 (2012) 31–39, doi:10.1016/j.msea.2012.02.024.

[80] L. Morsdorf, C.C. Tasan, D. Ponge, D. Raabe, 3D structural and atomic-scale analysis of lath martensite: effect of the transformation sequence, Acta Mater 95 (2015) 366–377, doi:10.1016/j.actamat.2015.05.023.